STUDIES ON LASERS AND LASER DEVICES

CO-PRINCIPAL INVESTIGATORS:

S.E. Harris
A.E. Siegman
J.F. Young

Final Report

for

NASA Grant NSG-2-44

National Aeronautics and Space Administration

Washington, DC

for the period

1 April 1980 - 31 March 1983

G.L. Report No. 3564

April 1983

Edward L. Ginzton Laboratory
W.W. Hansen Laboratories of Physics
Stanford University
Stanford, California 94305

TABLE OF CONTENTS

I. INTRODUCTION

The goal of this grant was to study lasers, laser devices, and novel uses of lasers to study physical phenomena. The active projects included the development of a tunable, narrowband XUV light source and its application to the spectroscopy of core-excited atomic states, and the development of a new technique for picosecond time-resolution spectroscopy of fast photophysical processes. These projects are described in more detail in the following sections.

II. SUMMARY OF RESEARCH

A. PICOSECOND MEASUREMENTS USING THE OPTOACOUSTIC DETECTION IN LIQUIDS WITH AN IMPROVED SAMPLE CELL

Staff: Jean-Marc Heritier

Research Supervised by Professor A.E. Siegman

Conventional *picosecond spectroscopy* uses either relatively complex detection apparatus (streak cameras, etc.) or stroboscopic two-pulse techniques to measure fast relaxation rates, generally in liquid or solid samples. Conventional *photoacoustic spectroscopy*, on the other hand, employs slowly chopped or pulsed light sources to measure weak absorptions in liquid, solid or gaseous samples by using the deposited heat energy to generate a detectable pressure wave. The first technique thus provides a powerful tool for measuring fast phenomena, while the latter is a simple, inexpensive and yet very sensitive technique of spectroscopy.

The work supported by this grant and which has been described in previous reports, has led to a new technique for accomplishing *picosecond* spectroscopy using the *photoacoustic* detection mechanism. In this two-pulse method, the photoacoustic signal is recorded as a function of delay between two ultrashort laser light pulses.

To carry out these experiments, we have designed and built a new photoacoustic cell for liquid samples which focused the pressure waves onto the receiving transducer for increased sensitivity. We found the ultimate sensitivity of this cell to be extremely good, so that an absorbed energy of $\sim$3 nJ could be detected by integration over 10 shots with a signal to noise of 1. While developed especially for these picosecond measurements, this cell may have wider uses in photoacoustics generally.

Extensive analysis of the pressure wave produced inside the liquid cell also led us to a complete and quantitative understanding of both the thermal and electrostrictive contributions to the pressure wave, and allowed us to predict the behavior of the photoacoustic cell under picosecond excitation.

Picosecond photoacoustic experiments on different dyes have been performed. We measured the excited state lifetimes of several molecular dyes with this technique. For the first time, a good measure of the excited-state-absorption cross

section at 1.061 μm of Rh6G and RhB is reported. Rotational effects have also been observed with Rh6G in heavy water and can be explained very well with a combined lifetime and rotational diffusion relaxation process.

We thus believe that the combined picosecond pulse plus photoacoustic detection method demonstrated in this research will become a useful and effective method for picosecond spectroscopy. This approach should be particularly applicable for measurements on weakly absorbing systems (such as dilute or expensive samples); for systems where excited-state fluorescence is not available as a detection mechanism; and for observations of weakly absorbing excited states in liquids or in solids. Much shorter laser pulses than used in our experiment are of course now available, and can equally well be used to gain greater time resolution. The use of more stable cw mode-locked lasers with greater pulse uniformity and higher repetition rate would substantially improve the signal averaging in the experiments, and further improvements in the cell design and electronics are also possible. The use of a tunable mode-locked dye laser would permit the determination of complete excited-state absorption spectra. Difficulties do arise, however, when the probe beam wavelength is short enough for the ground state absorption to become important.

To our knowledge, this is the first time that rotational relaxation effects have been observed on the excited-state absorption in organic dyes. These observations give useful information about the relative dipole orientation for the two absorption processes.

The research under this grant has resulted in a number of publications, including a Ph.D. dissertation just completed by J-M. Heritier.

B. DEVELOPMENT OF A TUNABLE, NARROWBAND XUV LIGHT SOURCE

Research Supervised by

Professors S.E. Harris and J.F. Young

The goal of this project is the development of a new light source in the extreme ultraviolet spectral region. The source is based upon the scattering of a tunable visible dye laser off an excited metastable atomic population (spontaneous anti-Stokes Raman scattering). The scattered photons have an energy equal to the sum of the storage energy and of the incident laser photon energy, are synchronous in time with the laser, and have a very narrow bandwidth determined by the convolution of the laser bandwidth and the Doppler width of the storage state.

Initial experiments have been made using helium as the storage species, producing radiation in the region of 54 nm with a resolution of 1.3 cm^{-1}. Tunability, however, was limited by the moderate brightness of the source and signal-to-noise considerations. The major efforts of the past year have concentrated on improving the source through a combination of increased storage population levels, improved collection geometry, and improved detection. We have also considered the use of other storage species in order to cover different spectral regions. These efforts have been quite successful, and the results are presented in a paper titled "Spontaneous Raman Scattering as a High Resolution XUV Radiation Source," which is to be published in a Special Issue of the *Journal of Quantum Electronics* devoted to the generation and use of XUV and soft x-ray radiation. A preprint of this paper is included as Appendix II.

III. PUBLICATIONS

[1] R.W. Falcone and G.A. Zdasiuk, "Pair absorption pumped barium laser," *Optics Lett.*, Vol. **5**, p. 155 (1980).

[2] S.E. Harris, R.W. Falcone, M. Gross, R. Normandin, K.D. Pedrotti, J.E. Rothenberg, J.C. Wang, J.R. Willison, and J.F. Young, "Anti-Stokes scattering as an XUV radiation source," in *Laser Spectroscopy V*, A.R.W. McKellar, T. Oka, and B.P. Stoicheff, eds. (New York: Springer-Verlag, 1981).

[3] J-M. Heritier, J.E. Fouquet, K. Jackson, and A.E. Siegman, "Picosecond photoacoustics using an elliptical acoustic cell," presented at 2nd International Topical Meeting on Photoacoustic Spectroscopy, University of California, Berkeley, California, June 22–25, 1981.

[4] J.E. Rothenberg, J.F. Young, and S.E. Harris, "High-resolution extreme-ultraviolet spectroscopy of potassium using Anti-Stokes radiation," *Optics Lett.*, Vol. **6**, p. 363 (August 1981).

[5] Jean-Marc Heritier, J.E. Fouquet, and A.E. Siegman, "Photoacoustic cell using elliptical acoustic focusing," *Appl. Opt.* **21**, pp. 90–93 (1982).

[6] A.E. Siegman, "Developments in mode-locked lasers and their applications," *Proceedings of SPIE*, Vol. **322**, pp. 60–67, 1982.

[7] P.M. Fauchet and A.E. Siegman, "Periodic ripple structures on semiconductors under picosecond pulse illumination," presented at 3rd Topical Meeting on Picosecond Phenomena, Garmisch-Partenkirchen, W.Germany, June 16–19, 1982.

[8] S.E. Harris, J.F. Young, R.W. Falcone, J.E. Rothenberg, and J.R. Willison, "Laser techniques for spectroscopy of core-excited atomic levels," in *Atomic and Molecular Physics Close to Ionization Thresholds in High Fields*, J.P. Connerade, J.C. Gay, and S. Liberman, eds. (France: Les Editions de Physique, 1982).

[9] Jean-Marc Heritier, "Electrostrictive limit and focusing effects in pulsed photoacoustic detection," *Opt. Comm.*, Vol. **44**, No. 4, pp. 267–272, 15 January 1983.

[10] J-M. Heritier, "Picosecond Spectroscopy using a Photoacoustic Detector,"

Ph.D. Dissertation, Stanford University, March 1983.

[11] J-M. Heritier and A.E. Siegman, "Picosecond time-resolved measurements using photoacoustic detection," to be presented at 3rd International Topical Meeting on Photoacoustic and Photothermal Spectroscopy, Paris, France, April 5–8, 1983.

[12] J-M. Heritier and A.E. Siegman, "Picosecond measurements using photoacoustic detection, *IEEE J. Quant. Electron.*, accepted for publication. See Appendix I.

[13] J.E. Rothenberg, J.F. Young, and S.E. Harris, "Spontaneous Raman scattering as a high resolution XUV radiation source," *IEEE J. Quant. Elect.* (to be published).

IV. APPENDIX I

PICOSECOND MEASUREMENTS USING PHOTOACOUSTIC DETECTION

Jean-Marc Heritier and A. E. Siegman
Department of Applied Physics
and
Edward L. Ginzton Laboratory
Stanford University
Stanford, California 94305

ABSTRACT

We report experimental results on picosecond spectroscopic measurements of excited-state cross sections, polarization properties, and lifetimes in organic dye solutions using a new technique for photoacoustic detection of the total photoacoustic impulse produced by two ultrashort optical pulses with variable time delay between them. The photoacoustic detection technique reported here appears to be a promising new way to observe weak excited-state cross sections, or to perform picosecond lifetime measurements in weakly absorbing and/or nonfluorescing optical systems.

PICOSECOND MEASUREMENTS USING PHOTOACOUSTIC DETECTION

Jean-Marc Heritier and A. E. Siegman

I. Introduction

Picosecond spectroscopy using ultrashort laser light pulses has now become an effective and successful tool for the measurement of ultrafast relaxation rates in many different physical systems [1]. At the same time, photoacoustic spectroscopy [2], in which one detects the thermo-acoustic signals produced by absorption of a laser beam in an absorbing sample, has become a similarly successful tool for measuring weak absorption lines in a variety of physical systems.

In an earlier publication [3] we proposed to combine the time resolution of picosecond spectroscopy with the simplicity and sensitivity of photoacoustic detection, by using a photoacoustic cell as the detection mechanism for picosecond pulse experiments. Photoacoustic detection by itself of course cannot achieve subnanosecond or picosecond time resolution. By observing the integrated photoacoustic response to two picosecond pulses with varying time delay, however, using a stroboscopic type of approach, one can measure fast relaxation processes with time resolution limited only by the optical pulse widths, even though the photoacoustic detection mechanism is much slower.

We have now carried out a preliminary experimental demonstration of this technique, with results which we report in this paper. Significant biological measurements made using a very similar technique have also been reported in the past year by Bernstein, Rothberg, and Peters [4]; and a similar type of time-resolved photoacoustic polarization spectroscopy has also been independently suggested by Hänsch [5].

In earlier papers we have already described an elliptical photoacoustic cell design which we developed for use in these experiments [3], and have also given an analysis of the acoustic impulse developed in a cylindrical geometry by a picosecond optical pulse (or a pair of closely spaced such pulses) [6]. In the present paper we first develop a simple theory based on rate equations to predict the photoacoustic signal behavior that will be measured versus inter-pulse delay in a stroboscopic

two-pulse experiment. We analyze both the case where the two light pulses have the same wavelength and the case where they have different wavelengths, and show the latter situation to be much more favorable.

We then present experimental results obtained with several different dyes excited with short pulses at 532 nm and 1.064 μm wavelengths from a mode-locked Nd:YAG laser. These results allow us to measure both the S_1 lifetime and the excited-state absorption cross-section at 1.064 μm of these dyes. Some rotational diffusion effects have also been experimentally demonstrated in a preliminary fashion for Rh6G using parallel or crossed polarizations for the two light pulses.

II. Theory

We propose to study molecules having a cross-section σ_1 from the ground state S_0 to S_1 at the wavelength λ_1 of a first or excitation light pulse, and a cross-section σ_2 from the excited state S_1 to higher levels S_1^* or S_n at the wavelength λ_2 of a second or probe pulse, as shown in Fig. 1. The special case where the two pulses have the same wavelength is also treated separately in Appendix A.

To analyse this system we start with six levels so as to describe accurately the saturation effects, but immediately simplify the algebra by assuming that the nonradiative decay rates γ_{54}, γ_{32} and γ_{10} are infinitely fast. We also assume that the decays from level 4 to levels 3 and 2 are completely nonradiative; a finite fluorescence quantum efficiency could be readily incorporated here, thereby reducing the photoacoustic signal generated along the 5→2 decay path. Similarly, the decay from level 2 to level 1 is assumed to be completely fluorescent. The frequency ω_{10} would have to be adjusted to account for any nonradiative part of the 2→0 decay.

The relevant rate equations under these conditions are reduced to

$$\frac{dN_4}{dt} = \left(\frac{\sigma_2 I_2}{\hbar\omega_2}\right) N_2 - \gamma_4 N_4 \tag{1}$$

and

$$\frac{dN_2}{dt} = \left(\gamma_4 - \frac{\sigma_1 I_1}{\hbar\omega_1}\right) N_4 - \left(\gamma_{21} + \frac{\sigma_1 I_1}{\hbar\omega_1} + \frac{\sigma_2 I_2}{\hbar\omega_2}\right) N_2 + \left(\frac{\sigma_1 I_1}{\hbar\omega_1}\right) N \tag{2}$$

where I_1 and I_2 are the instantaneous intensities at λ_1 and λ_2; $N = N_0 + N_2 + N_4$ is the total population; and $\gamma_4 = \gamma_{43} + \gamma_{42}$ is the total downward decay rate from level 4. Equations (1) and (2) can be solved easily for constant intensities I_1 and I_2 to give

$$N_4(t) = \frac{N}{D}\frac{\sigma_2 I_2}{\hbar\omega_2} + A\frac{\sigma_2 I_2}{\hbar\omega_2}\exp(\lambda_a t) + B\frac{\sigma_2 I_2}{\hbar\omega_2}\exp(\lambda_b t) \tag{3}$$

and

$$N_2(t) = \frac{N}{D}\gamma_4 + A(\gamma_4 + \lambda_a)\exp(\lambda_a t) + B(\gamma_4 + \lambda_b)\exp(\lambda_b t) \tag{4}$$

where $D = \gamma_4 + \sigma_2 I_2/\hbar\omega_2 + \gamma_{21}\gamma_4\hbar\omega_1/\sigma_1 I_1$. The eigenvalues λ_a and λ_b with signals present are given by

$$\lambda_a, \lambda_b = -\tfrac{1}{2}(\gamma_{21} + \gamma_4 + \sigma_1 I_1/\hbar\omega_1 + \sigma_2 I_2/\hbar\omega_2) \pm \tfrac{1}{2}\sqrt{\Delta}$$

where

$$\Delta = \left(\gamma_4 - \gamma_{21} + \frac{\sigma_2 I_2}{\hbar\omega_2} - \frac{\sigma_1 I_1}{\hbar\omega_1}\right)^2 + \frac{4\gamma_{21}\sigma_2 I_2}{\hbar\omega_2}$$

and the constants A and B depend upon initial conditions.

We assume that the nonradiative relaxation energies are immediately transferred into heating of the surrounding medium. Hence at any instant t the amount of heat energy H deposited in the medium per unit volume and per unit time will be

$$\frac{dH}{dt} = \left[\frac{\sigma_1 I_1}{\hbar\omega_1}N(t) + \left(\frac{\omega_{10}\gamma_{21}}{\omega_{32}} - \frac{\sigma_1 I_1}{\hbar\omega_1} + \frac{\omega_{54}}{\omega_{32}}\frac{\sigma_2 I_2}{\hbar\omega_2}\right)N_2(t) + \left(\frac{\omega_{42}\gamma_4}{\omega_{32}} - \frac{\sigma_1 I_1}{\hbar\omega_1}\right)N_4(t)\right]\hbar\omega_{32} \tag{5}$$

In order to simulate a two-pulse sequence, we now assume that the light intensity at wavelength λ_1 is on from $t = 0$ to $t = \tau_1$; the system is left to partially relax from $t = \tau_1$ to $t = \tau$; and then the light intensity at wavelength λ_2 is on from $t = \tau$ to $t = \tau + \tau_2$. At time $t = 0$, before the λ_1 pulse arrives, all the dye population is in the ground state, i.e., $N_0 = N$. Since the time scale of the whole process,

successive illumination plus relaxation, is less than the acoustic propagation time across the beam (~20 ns at most compared to 50 ns at least) [6], the acoustic signal will be proportional to the total heat deposited during the two-pulse excitation. We can write separate solutions for two cases of experimental interest, depending on whether the decay rate γ_{21} of the first excited singlet level is slow or fast compared to the pulsewidths:

1) If we assume that the pulses are short and intense, so that $\gamma_{21}\tau_1 \ll (\sigma_1 E_1/\hbar\omega_1)$, and that γ_4 is very fast so that $\gamma_4\tau_2 \gg (\sigma_2 E_2/\hbar\omega_2)$, then the photoacoustic signal voltage PAS as a function of pulse delay τ becomes

$$\mathrm{PAS} = KN[1-\exp(-E_1/E_{1S})][\omega_{32}+\omega_{10}+(E_2/E_{2S})\omega_{52}\exp(-\gamma_{21}\tau)] \quad (6)$$

where E_1 and E_2 are the energy fluences of the two light pulses; E_{1S} and E_{2S} are the saturation energies $\hbar\omega_1/\sigma_1$ and $\hbar\omega_2/\sigma_2$; and K is a constant factor that accounts for the cell geometry and the detector sensitivity.

We see that the photoacoustic signal is made up of a constant background, caused by the E_1 pulse and independent of the pulse delay, plus an exponentially decaying part proportional to $\sigma_2 E_2$. The ratio of these two quantities will be

$$R = \frac{\sigma_2 E_2}{\hbar(\omega_{32}+\omega_{10})} \quad (7)$$

where we used the fact that $\omega_{52} = \omega_2$. This ratio can be measured experimentally and thus used to determine the excited-state absorption coefficient σ_2. Note that this ratio will not depend upon the light pulse energy E_1 at λ_1, which can be weak or on the contrary can completely saturate the ground state absorption. In either case, the photoacoustic signal will be proportional to the excited state initial population $N[1-\exp(-E_1/E_{1S})]$ created by the light pulse at λ_1, but the ratio R will be independent of E_1.

2). When γ_4 is very fast so that $\gamma_4\tau_2 \gg E_2/E_{2S}$ and $\gamma_4 \gg \gamma_{21}$, another situation of interest is obtained if γ_{21} is very fast so that $\gamma_{21}\tau_1 \gg 1$ and $\gamma_{21}\tau_2 \gg 1$. In this case the photoacoustic signal again is the sum of a constant background plus a delay dependent term which decays as $\exp(-\gamma_{21}\tau)$. The ratio of these two terms

for zero delay ($\tau = 0$) can be found to be:

$$R = \frac{1}{\gamma_{21}^2 \tau_1 \tau_2} \frac{\sigma_2 E_2}{\hbar(\omega_{32} + \omega_{10})} \tag{8}$$

The ratio R found for slow decay of the excited state (Eq. 7) is now divided by the dimensionless factor $\gamma_{21}^2 \tau_1 \tau_2$ when γ_{21} is large. Small ratios R will therefore be measured if the absorption cross-section σ_2 is small and/or if the decay rate of the excited state γ_{21} is fast.

The case where the two pulses have the same wavelength λ_1 is treated separately in Appendix A.

III. Experimental Results

A. Single-Pulse Saturation Experiments

In order to verify that saturation and excited-state absorption effects could in fact be observed, we first carried out a small number of experiments with our apparatus using only one pulse at 532 nm, and recording the photoacoustic signal along with the transmitted energy for different values of the incident energy. The theory for this case is developed in Appendix A. These experiments used 80 ps long light pulses with total energy of up to 5 μJ maximum focused to a spot size $w_0 = 100$ μm in our elliptical photoacoustic cell. A similar setup used for two-pulse experiments is described in detail later.

Some typical early single-pulse results obtained with the dye rubrene in benzene are shown in Fig. 2. We observe that for input energies above the saturation energy $E_{1S} = \hbar\omega/\sigma_1 \approx 7.7$ mJ/cm^2 that can be calculated using the published [7] value for σ_1 of rubrene (42×10^{-18}cm^2 at 532 nm), the photoacoustic signal begins to increase in more than linear fashion, even though the transmitted optical energy increases in essentially linear fashion and shows no strong evidence for saturation of the $S_0 \rightarrow S_1$ transition.

We interpret these results as arising from partial saturation of the $S_0 \rightarrow S_1$ transition, followed by excited-state absorption of the 532 nm pulse from the S_1 level. Absorption from the excited state would be expected to produce relatively more photoacoustic signal than absorption from the S_0 ground state, both because

nonradiative relaxation rates from higher levels are expected to be stronger than from the largely fluorescent S_1 level, and because the energy gap involved is larger. Note that more careful measurements of this type of data using a more stable laser could permit measurements of saturation intensities that are difficult to see optically, as well as possible measurements of excited state cross sections, without the use of any optical detector. A similar approach has also been used earlier, with much longer pulses, by Razumova and Starobogatov [8].

Similar nonlinearities in the photoacoustic response versus input pulse energy were also observed for Rhodamine B in ethanol and for the food dye Red #40 in ethanol. For these solutions, however, the photoacoustic signal per unit input energy decreased with increasing input energy fluence. We interpret this as arising from saturation of the ground state absorption, without producing excited-state absorption at the same wavelength. However, further detailed information was difficult to obtain from these preliminary results.

In order to complement these preliminary results, a two-pulse experiment with two 532 nm pulses was attempted on a solution of rubrene in benzene. However, this experiment was not successful in exhibiting a delay dependent photoacoustic signal. The expected contrast between the constant background and the exponentially decaying part of the signal was only predicted to be about 8×10^{-2}, based on the nonlinearity of the photoacoustic signal versus input energy curve of Fig. 2 and the analysis of Appendix A. Furthermore, the 16.5 ns excited-state lifetime of rubrene [7] is so long that only partial excited-state relaxation could be reached with our 10 ns delay line. The data was therefore hidden in long term noise variations and delay line misalignment problems.

B. Two-Pulse Experimental Apparatus

As was pointed out earlier, a two-pulse experiment using two different wavelengths λ_1 and λ_2 can have a much better contrast than a single-wavelength experiment. Such as experiment should yield important information on the short-lived excited states of various dyes and their absorption cross section at the probe wavelength λ_2.

The setup used to demonstrate this experimentally is shown in Fig. 3. A cw-pumped, repetitively Q-switched and mode-locked Nd:YAG laser produces bursts

of about twenty mode-locked pulses that are ~100 ps in duration and separated from each other by the roundtrip time $T \simeq 4.8$ ns, at an adjustable repetition rate of 30 to 100 bursts per second. A $LiNbO_3$ Pockels cell selects the most intense (50 μJ) pulse of each burst, which is then frequency-doubled in an angle-tuned CD*A crystal. The green radiation is then separated from the remaining infrared and sent through a mechanical delay line controlled by a computer.

The infrared beam is sent along a separate optical path with fixed delay, and both beams are focused into the photoacoustic cell from opposite sides to the same spot size of ~70 μm. The resulting photoacoustic signal is preamplified inside the shielded housing that contains the photoacoustic cell, then amplified and sent to an 8-channel Sample and Hold electronic device. Three photodiodes D_3, D_2, and D_1 monitor respectively the energy of the green pulse (E_{532}), the energy of the infrared pulse (E_{1064}) and the energy in the green produced by a nonsaturated $LiIO_3$ crystal which doubles a small part of the original infrared pulse (ENS_{532}). These signals are also sent to the Sample and Hold device and the computer reads them along with the photoacoustic signal after each laser pulse.

Monitoring of the effective pulse width as obtained by E^2_{1064}/ENS_{532} on each shot is necessary to monitor the shot-to-shot operation of our somewhat unstable single-pulse selector. The laser repetition rate of 40 Hz in most experiments is limited largely by the data acquisition process. Mechanical shutters, controlled by the computer, are located in the optical path of each beam. These allow us to find the delay-independent part of the photoacoustic signal due to the 532 nm beam alone, caused primarily by ground state absorption in the dye under study; or the delay-independent component due to the 1064 nm beam alone. Since the 1064 nm wavelength is not significantly absorbed by the ground state in the dyes we studied, the latter signal comes primarily from absorption of the IR wavelength in the solvents employed.

The spatial alignment of the two beams is realized by first removing the photoacoustic cell, then positioning a 50 μm pinhole at the focal spot of one beam and optimizing the transmission of the other. The 532 nm beam in the delay line is collimated with a spot size $w = 1.3$ mm and a Rayleigh range $z_R = 10$ m which ensures that no defocusing will take place when the delay line increases the optical path by a maximum of 3 m. A typical experiment lasts from 5 minutes to 1 hour

and the data, immediately displayed on the computer console, are also permanently stored for later analysis.

C. Two-Pulse Experimental Results

Our first experiment was performed on Rhodamine 6G dye dissolved in ethanol with a molarity of $1.8\times10^{-3}\mathrm{M}/\ell$ and an absorption coefficient $\alpha = 0.43\ \mathrm{cm}^{-1}$ at 532 nm. Figure 4 shows the delay-dependent photoacoustic signal produced by both the 532 nm and 1064 nm pulses arriving in the sample. As expected, this signal is very close to zero when the delay is negative because the 1064 nm pulse, arriving before the 532 nm pulse, does not see any excited state, and therefore the two pulses are completely decoupled. For positive delays, however, the signal is large and proportional to the exponentially decaying excited state population. When the delay is larger than about 4.8 ns, a second jump in the photoacoustic signal is observed. This is due to the (undesired) transmission by the Pockels-cell pulse selector of a second, less intense pulse after the main one. When the probing pulse delay is larger than the roundtrip time T of the laser oscillator, the main 1064 nm pulse is able to probe additional new excited state population created by this second pulse.

The bottom of Fig. 4 shows the same data plotted on a logarithmic scale. It verifies that the decay is exponential with a lifetime $\tau = \gamma_{21}^{-1} \approx 3.7 \pm 0.2$ ns, in good agreement with the published data [7].

The delay-dependent signal shown in Fig. 4 rides on top of a delay-independent signal produced by the two pulses acting separately. The background due to the S_0 to S_1 absorption of the 532 nm pulse alone is approximately twice as large; and the background due to the solvent absorption of the 1064 nm pulse is about 10 times larger.

The complete photoacoustic signal, including the constant background part due to the ground state absorption in Rh6G of the 532 nm pulse, was also used to compute the ratio R given by Eq. (7). The total energy at 1064 nm in each pulse was 15 μJ. Assuming $\omega_{32} + \omega_{10}$ to be the difference between the 532 nm frequency and the frequency of a fluorescence photon at 590 nm, the excited state cross section can be easily calculated, and is given in Table 1.

We also studied a 3.2×10^{-6} M/ℓ solution of Rhodamine B in ethanol with an absorption coefficient of $\alpha = 0.36$ cm^{-1} at 532 nm. Figure 5 shows the data obtained for this dye. The same comments that were made for Rhodamine 6G apply to this experiment. The decay time is found to be $\tau = \gamma_{21}^{-1} = 3.30 \pm 0.15$ ns, in good agreement with the value of 3.2 ns published in Ref. [7], but a bit too long compared to the value of 2.9 ns published in Ref. [9].

The excited-state cross section was again deduced from the ratio of the exponential portion to the constant background due to the 532 nm pulses alone, assuming again that the $2 \rightarrow 1$ decay is purely fluorescent at 590 nm. The resulting excited-state cross sections are given in Table 1.

Table 1 – Measured Excited-State Cross Sections at 1064 nm

Excited state Cross Section	Solvent	Dye
$\sigma_2 = 36 \pm 20 \times 10^{-20}$cm^2	Ethanol	Rh6G
$\sigma_2 = 15 \pm 10 \times 10^{-20}$cm^2	Ethanol	RhB
$\sigma_2/\gamma_{21}^2 < 5 \times 10^{-40}$cm^{2}s^2	Heavy Water	RED#40

Finally we did the same kind of experiment with the food dye Red #40 in heavy water. (Heavy water was used to minimize the background absorption of the 1.064 μm pulses). No delay-dependent signal could be seen above the background noise fluctuations in this experiment, however. It is believed the main reason for this is the extremely fast and mainly nonradiative decay γ_{21} in this dye (almost no fluorescence is emitted from the sample when illuminated by 532 nm pulses). Assuming $\omega_{32} + \omega_{10}$ is the frequency of radiation of 532 nm wavelength and taking $\tau_1 = 80$ ps, $\tau_2 = 100$ ps, an upper limit for the ratio σ_2/γ_{21}^2 can be found using Eq. 8, as given in Table 1.

Each excited-state cross section given in Table 1 is the result of several runs and the quoted uncertainty is mainly due to experimental errors including beam misalignment. (If the 1064 nm pulse does not probe the exact region excited by the 532 nm pulse, the absorption will be reduced and the cross section will be underestimated). There are of course also uncertainties which arise from the fact that the real molecular system may be more complex than our analytical model.

Our data does not agree well with the excited-state cross section of $\sigma_2 \approx 2.2 \times 10^{-17}$ cm^2 for Rhodamine 6G at 1064 nm given in Ref. [10]. These quite different experiments may very well be probing different properties of the excited state, and thus agreement is not necessarily to be expected.

D. Rotational Relaxation and Polarization Experiments

It is well known [11,12,13] that an ensemble of randomly aligned molecules, such as Rhodamine 6G in solution, when excited by a linearly polarized light beam, will exhibit an anisotropy in its excited-state absorption. This is due to preferential excitation of those molecules whose transition dipole moment is oriented along the excitation E field. If a light pulse is sent to probe the excited state population immediately following a linearly polarized excitation pulse, this probe pulse will see a different absorption if its polarization is parallel to the excitation beam polarization or perpendicular to it. The anisotropic excited-state population density will relax or diffuse back into an isotropic distribution with an orientational relaxation time, at the same time as the regular population decay from the excited state takes place

The excited state absorption of radiation whose polarization is parallel or perpendicular to the excitation pulse polarization should vary as follows:

$$\alpha = \alpha_0 \{\exp(-\gamma_{21} t) + \beta \exp[-(\gamma_{21} + 1/\tau_{rot})t]\} \tag{9}$$

where α_0 is the isotropic part of the initial absorption at time $t = 0$, γ_{21} is the population decay rate, τ_{rot} is the rotational diffusion time, and $\beta = 4/5$ for parallel polarizations and $\beta =$ -2/5 for perpendicular polarizations, assuming that the directions of the dipole moments of the transitions $S_n \leftarrow S_1$ and $S_1 \leftarrow S_0$ are parallel [14].

To study these rotational effects, we performed picosecond photoacoustic measurements like those described above on a solution of Rhodamine 6G in heavy water plus 2% Ammonyx LO, using different polarizations of the 1064 nm probe pulse relative to the 532 nm excitation pulse. Heavy water was used because of its negligible absorption at 1064 nm in contrast with water and most of the organic solvents. To get a better signal to noise ratio, we also eliminated the single pulse selector and used the entire train of mode-locked pulses. A half wave plate was used

in the 532 nm beam to rotate its polarization and a polarizer in each beam selected the desired linear polarization.

The results are shown in Fig. 6, in which the delay-dependent part of the photoacoustic signal is plotted versus delay with the polarizations of the 532 nm and the 1064 nm beams either crossed or parallel. Because the entire mode-locked train was used, the signal is nonzero for negative delays, i.e., the n-th 1064 nm pulse still sees some excited states created by the $(n-1)$-th 532 nm pulse that came about 5 ns before. For slightly positive delays, the striking difference in the signal amplitude for the two curves demonstrates the strong absorption anisotropy.

The initial slope of the decay curve at time $t = 0+$ (just after an excitation pulse) for the population probed by a 1064 nm beam with its polarization parallel or perpendicular to the excitation beam polarization can be calculated to be

$$\left(\frac{dn}{dt}\right)_{t=0+} = -\gamma_{21} n_0 \left[1 + \beta\left(1 + \frac{1}{\gamma_{21}\tau_{rot}}\right)\right] \tag{10}$$

As expected, the decay rate for the parallel polarization case ($\beta = 4/5$) is much larger than for the perpendicular polarization case ($\beta = -2/5$). Our experimental results, although rather crude and noisy, fit very well with an expected population decay time of 4.1 ± 0.2 ns and a rotational decay time $\tau_{rot} = 2.5 \pm 0.5$/ ns, both in agreement with published data [9,11,12]. As reported earlier [11,12], this rotational decay time is long compared to the rotational decay times for solutions in ethanol or methanol because the Rhodamine 6G molecule is bonded to a large micelle soap complex in water. Our measurements also confirm directly that the dipole moments of the transitions $S_n \leftarrow S_1$ and $S_1 \leftarrow S_0$ are parallel [14].

V. Conclusions

We believe that the combined picosecond pulse plus photoacoustic detection method demonstrated in this paper will become a useful and effective method for picosecond spectroscopy. This approach should be particularly applicable for measurements on weakly absorbing systems (such as dilute or expensive samples); for systems where excited-state fluorescence is not available as a detection mechanism; and for observations of weakly absorbing excited states in liquids

or in solids. Much shorter laser pulses than used in our experiment are of course now available, and can equally well be used to gain greater time resolution. The use of more stable cw mode-locked lasers with greater pulse uniformity and higher repetition rate would substantially improve the signal averaging in the experiments, and further improvements in the cell design and electronics are also possible. The use of a tunable mode-locked dye laser would permit the determination of complete excited-state absorption spectra. As was pointed out in this study, difficulties do arise when the probe beam wavelength is short enough for the ground state absorption to become important.

To our knowledge, this is the first time that rotational relaxation effects have been observed on the excited-state absorption in organic dyes. These observations give useful information about the relative dipole orientation for the two absorption processes.

Note that most conventional methods of picosecond spectroscopy using pulse and probe methods are susceptible to coherent artifacts, or induced grating effects, when the "excite" and the "probe" pulses are coincident in time. These effects should not exist when the photoacoustic detection is used because of its purely thermal nature.

Appendix A. Analysis of Single-Wavelength Case

In some situations one may want to study the excited state absorption cross-section of a sample at the same wavelength λ_1 as the one used for the excitation from the ground state. Equations (1) through (4) will still be valid if we replace I_2 and ω_2 by I_1 and ω_1, respectively.

We first assume that the two light pulses are coincident in time ($\tau = 0$), have a total intensity I at the wavelength λ for some duration τ_1, and are turned off thereafter. As before, the decay rate γ_4 is assumed to be very fast. The photoacoustic signal will then be:

$$\mathrm{PAS}(E,\tau=0) = KN\frac{E/E_{1S}}{\gamma_{21}\tau_1 + E/E_{1S}}\left\{(\omega_{32}+\omega_{10})\gamma_{21}\tau_1 + \omega_{52}\frac{E}{E_{2S}} + \frac{1-\exp(-\gamma_{21}\tau_1 - E/E_{1S})}{\gamma_4\tau_1 + E/E_{1S}}\left[(\omega_{32}+\omega_{10})\frac{E}{E_{1S}} - \omega_{52}\frac{E}{E_{2S}}\right]\right\} \tag{A.1}$$

where E is the total energy fluence in the two pulses. This photoacoustic signal is plotted on Fig. 7 versus E/E_{1S} for different values of $E_{1S}/E_{2S} = \sigma_2/\sigma_1$ and $\gamma_{21}\tau = 0.025$. It is interesting to note that for the special case of $\sigma_2/\sigma_1 = (\omega_{32} + \omega_{10})/\omega_{52}$, the photoacoustic signal simplifies to

$$\mathrm{PAS}(E, \tau = 0) = KN\frac{E}{E_{1S}}(\omega_{32} + \omega_{10}) \qquad (A.2)$$

i.e., the photoacoustic signal is linear in E.

Now when the two light pulses are separated by a large delay the second pulse will not see any excited molecules, since they will have decayed back to the ground level. Therefore the second light pulse will add up to the photoacoustic signal created by the first one in a completely independent fashion. Assuming both pulses have equal energy $E/2$, the photoacoustic signal will be:

$$\mathrm{PAS}(E, \tau \to \infty) = 2\mathrm{PAS}(E/2, \tau = 0) \qquad (A.3)$$

Therefore there will not be any change in the photoacoustic signal when the delay between the two pulses is varied if $\mathrm{PAS}(E, \tau = 0)$ is a linear function of E. The photoacoustic signal will only change with varying delay when $\mathrm{PAS}(E, \tau = 0)$ is a nonlinear function of E.

A good measure of the photoacoustic changes when the delay is varied is the contrast coefficient defined as follows:

$$R = \frac{|\mathrm{PAS}(E, \tau = 0) - \mathrm{PAS}(E, \tau \to \infty)|}{\mathrm{Min}[\mathrm{PAS}(E, \tau = 0), \mathrm{PAS}(E, \tau \to \infty)]} \qquad (A.4)$$

where the denominator is the minimum of the two values $\mathrm{PAS}(E, \tau = 0)$ and $\mathrm{PAS}(E, \tau \to \infty)$. This quantity is fully equivalent to the ratio R we defined earlier (Eqs. (7) and (8)) and therefore will have the same notation.

This contrast ratio R is plotted in Fig. 8 versus E/E_{1S} for different values of σ_2/σ_1 and $\gamma_{21}\tau = .025$. As expected, the contrast has a maximum value of 1 only for a certain range of values for E/E_{1S} and only for σ_2/σ_1 sufficiently different from $(\omega_{32} + \omega_{10})/\omega_{52}$. For $\sigma_2/\sigma_1 = (\omega_{32} + \omega_{10})/\omega_{52}$, as expected from the linearity of Eq. (A.2), the contrast is null for all values of E/E_{1S}.

Acknowledgement

Different parts of this work were supported by the National Aeronautics and Space Administration, and by the Air Force Office of Scientific Research.

REFERENCES

[1] "Ultrashort Light Pulses: Picosecond Techniques and Applications," edited by S. L. Shapiro, Springer-Verlag, Berlin, 1977.

[2] A good introduction and many additional references to the subject can be found in "Photoacoustics and Photoacoustic Spectroscopy," by Allan Rosencwaig, John Wiley & Sons (1980). Also, see C.K.N. Patel and A.C. Tam, "Pulsed optoacoustic spectroscopy of condensed matter," *Rev. of Mod. Phys.* **53**, 517–550 (1981).

[3] Jean-Marc Heritier, J.E. Fouquet, and A.E. Siegman, "Photoacoustic cell using elliptical acoustic focusing," *Appl. Opt.* **21**, pp. 90–93 (1982).

[4] M. Bernstein, L.J. Rothberg, and K.S. Peters, "Picosecond Time-Resolved Photoacoustic Spectroscopy," in *Picosecond Phenomena III*, edited by K.B. Eisenthal, R.M. Hochstrasser, W. Kaiser, and A. Laubereau (Springer-Verlag, Berlin, 1982); pp. 112–115.

[5] Professor T. Hänsch, Department of Physics, Stanford University, private communication.

[6] Jean-Marc Heritier, "Electrostrictive limit and focusing effects in pulsed photoacoustic detection," *Opt. Comm.*, to be published.

[7] Isadore B. Berlman, *Handbook of Fluorescence Spectra of Aromatic Molecules*, Second Edition, Academic Press (1971).

[8] T.K. Razumova and I.O. Starobogatov, "Investigation of the light quenching of luminescence using a photoacoustic detection technique," *Opt. Spectrosc. (USSR)* **42**, 274-277 (1977).

[9] J.M. Harris and F.E. Lytle, "Measurement of subnanosecond fluorescence decays by sampled single-photon detection," *Rev. Sci. Instrum.* **48**, 1469–1467 (1977).

[10] I.O. Starobogatov, "Photoacoustic spectroscopy of transitions from excited states of dye molecules," *Opt. Spectrosc. (USSR)* **46**, 455–457 (1979).

[11] Donald W. Phillion, Dirk J. Kuizenga, and A.E. Siegman, "Subnanosecond relaxation time measurements using a transient induced grating method," *Appl. Phys. Lett.* **27**, 85–87 (1975).

[12] D.W. Phillion, D.J. Kuizenga, and A.E. Siegman, "Rotational diffusion and triplet state processes in dye laser solutions," *J. Chem. Phys.* **61**, 3828-3839 (1974).

[13] A.E. Siegman, D.W. Phillion, and D.J. Kuizenga, "Rotational relaxation and triplet state effects in the CW dye laser," *Appl. Phys. Lett.* **21**, 345-348 (1972).

[14] V.L. Bogdanov and V.P. Klochkov, "Hot luminescence and vibrational relaxation in complex molecules with diffuse spectra," *Opt. Spectrosc. (USSR)*, **44**, 412-416 (1978).

CAPTIONS FOR FIGURES

Figure 1.

Energy level system used to analyse picosecond photoacoustic experiments. The decay rates γ_{54}, γ_{32}, and γ_{10} are assumed to be infinitely fast, and all decay paths are nonradiative except from 2 to 1. If λ_2 is different from λ_1, we assume that the second pulse at wavelength λ_2 is not absorbed by the ground state population N_0 and that the first pulse at wavelength λ_1 is not absorbed by the excited state population N_2.

Figure 2.

Photoacoustic signal voltage and transmitted optical energy versus input single-pulse energy fluence through a weakly absorbing solution of rubrene in benzene.

Figure 3.

Experimental setup used for two-pulse photoacoustic experiments. Mirrors $M1$ and $M2$ are the laser oscillator mirrors; I is an intracavity iris for transverse mode selection; and QS and ML are the acousto-optic Q-switch and mode-locker. The box labelled PC is the $LiNbO_3$ Pockels cell; $DM1$ and $DM2$ are dichroic mirrors; F_1 and F_3 are infrared blocking filters; and F_2 is a long pass filter. Lenses $L1$ and $L2$ are 50 cm focal-length lenses; $P1$ and $P2$ are two calcite polarizers; and $D1$, $D2$ and $D3$ are PIN diodes. The two shutters $S1$ and $S2$ are computer controlled, and the Sample and Hold electronics are connected to a DEC MINC 11/03 minicomputer.

Figure 4.

Delay-dependent part of the photoacoustic signal versus delay of the 1064 nm pulse with respect to the 532 nm pulse, for measurements on Rhodamine 6G in ethanol. Linear scale is used at the top and logarithmic scale at the bottom.

Figure 5.

Results similar to Fig. 4, but for a solution of Rhodamine B in ethanol.

Figure 6.

Picosecond photoacoustic results for a solution of Rhodamine 6G in heavy water with 2% Ammonyx LO versus time delay of the 1064 nm pulse relative to the

532 nm pulse. On each plot, one curve is obtained with parallel linear polarizations for the 532 nm and the 1064 nm beams, and the other is obtained with crossed polarizations.

Figure 7.

Theoretical photoacoustic signal versus input energy, normalized to $E_{s1} \equiv \hbar\omega/\sigma_1$, for different values of the ratio σ_2/σ_1. We assume that $\gamma_{21} \times \tau = 0.025$ and that $(\omega_{32} + \omega_{10})/\omega_{52} = 9.83 \times 10^{-2}$.

Figure 8.

Theoretical contrast ratio versus total input energy, normalized to $E_{s1} \equiv \hbar\omega/\sigma_1$ in a two-pulse single-wavelength experiment for different values of the ratio σ_2/σ_1. We assume that $\gamma_{21} \times \tau = 0.025$ and that $(\omega_{32} + \omega_{10})/\omega_{52} = 9.83 \times 10^{-2}$.

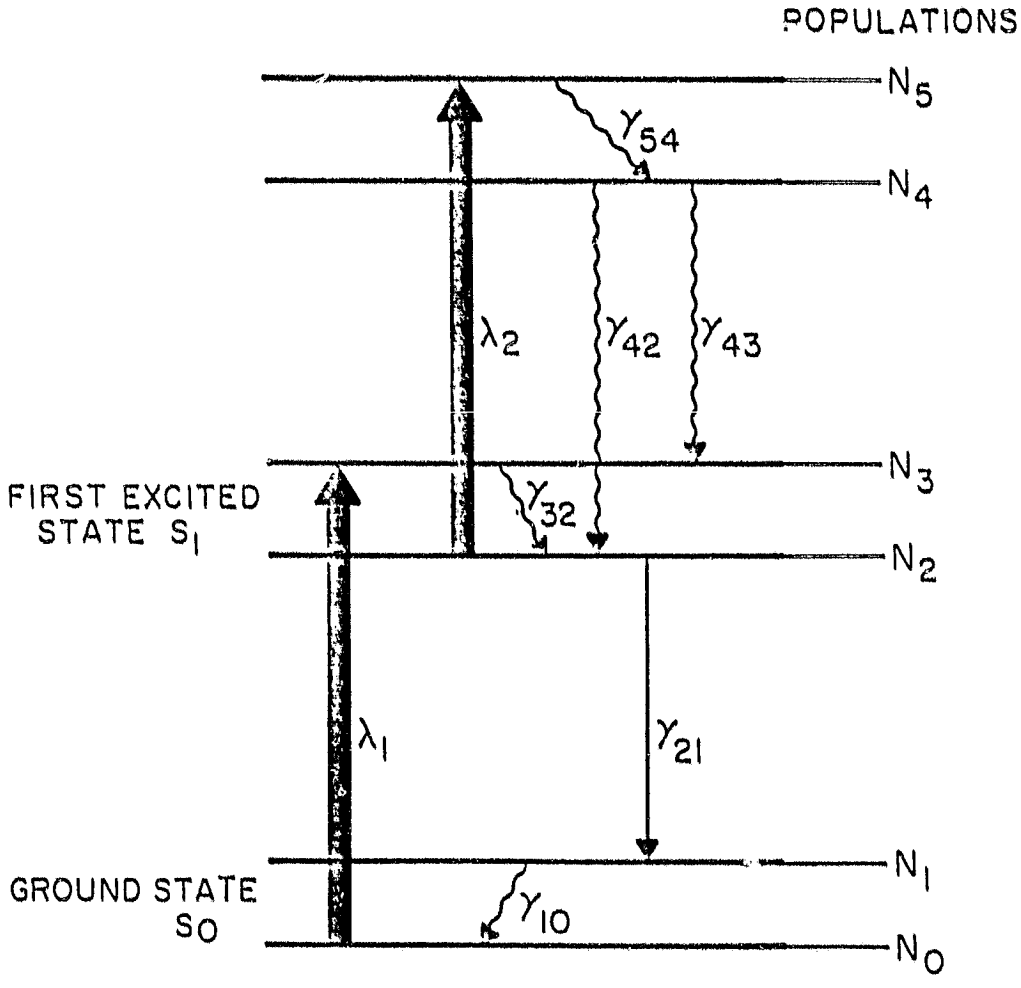

Figure 1

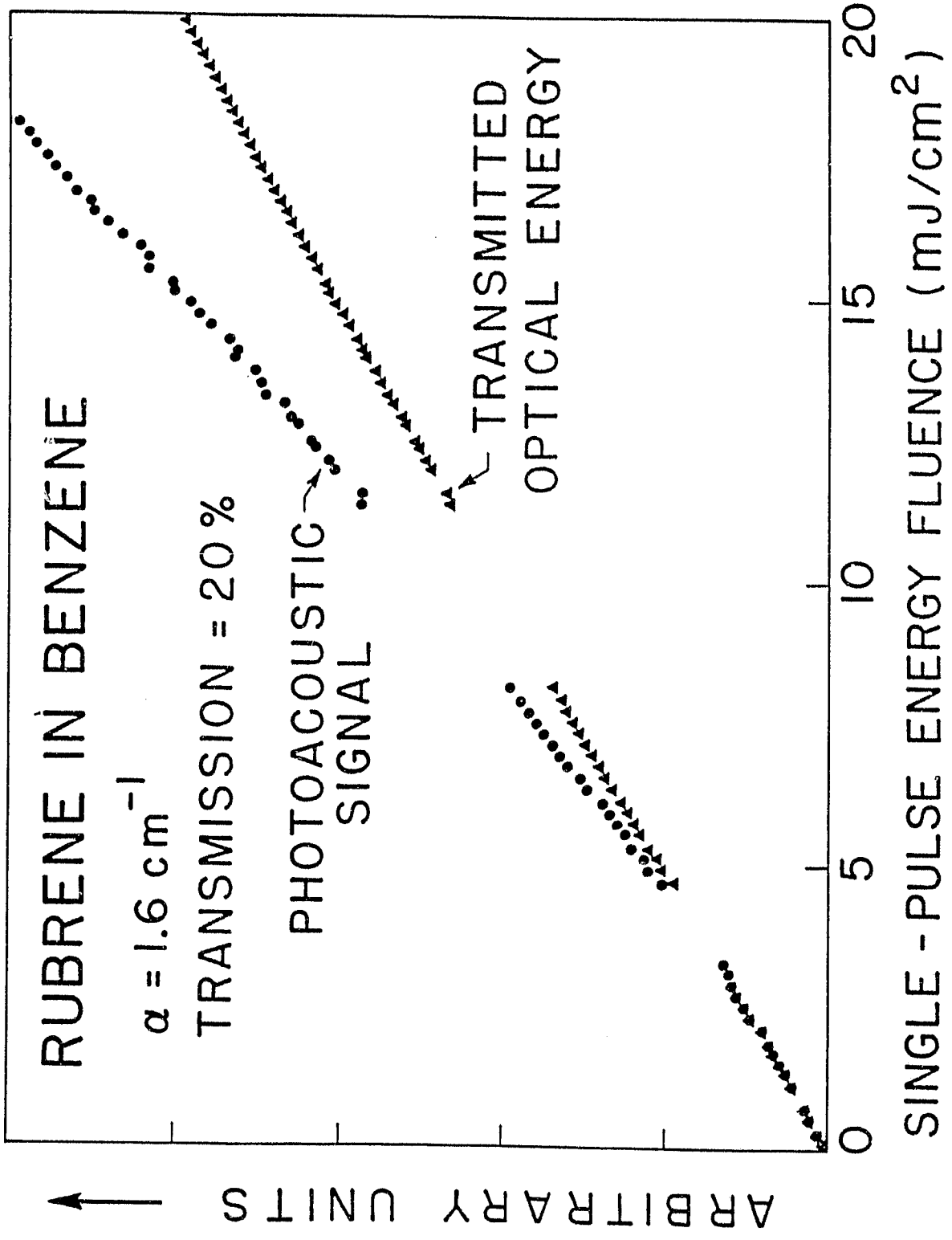

Figure 2

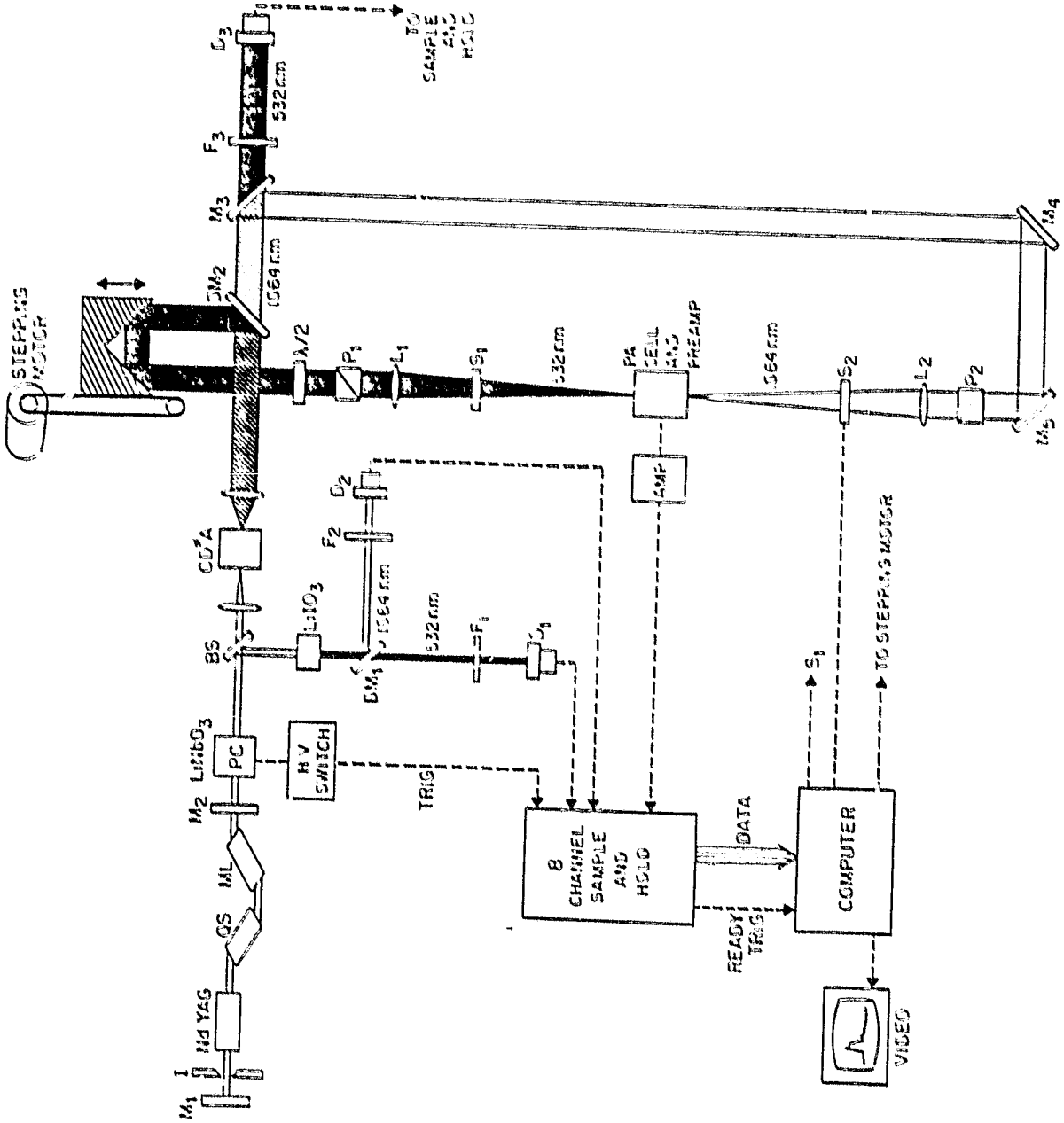

Figure 3

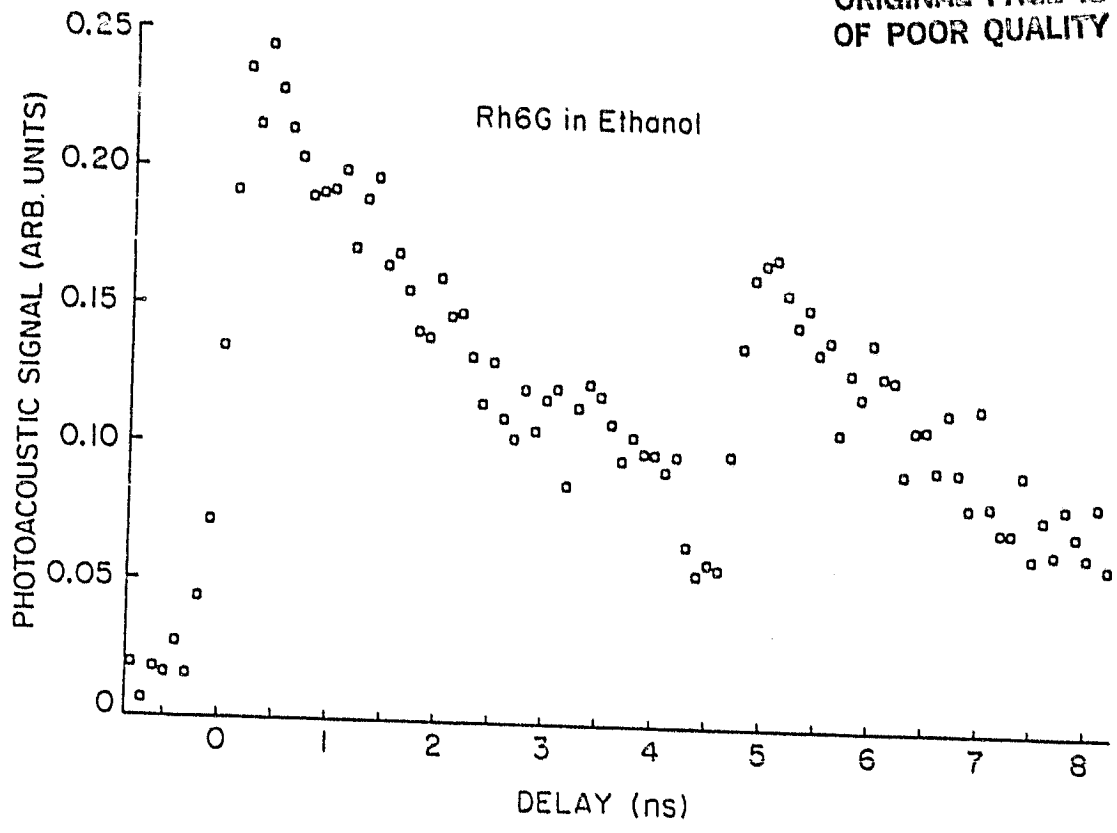

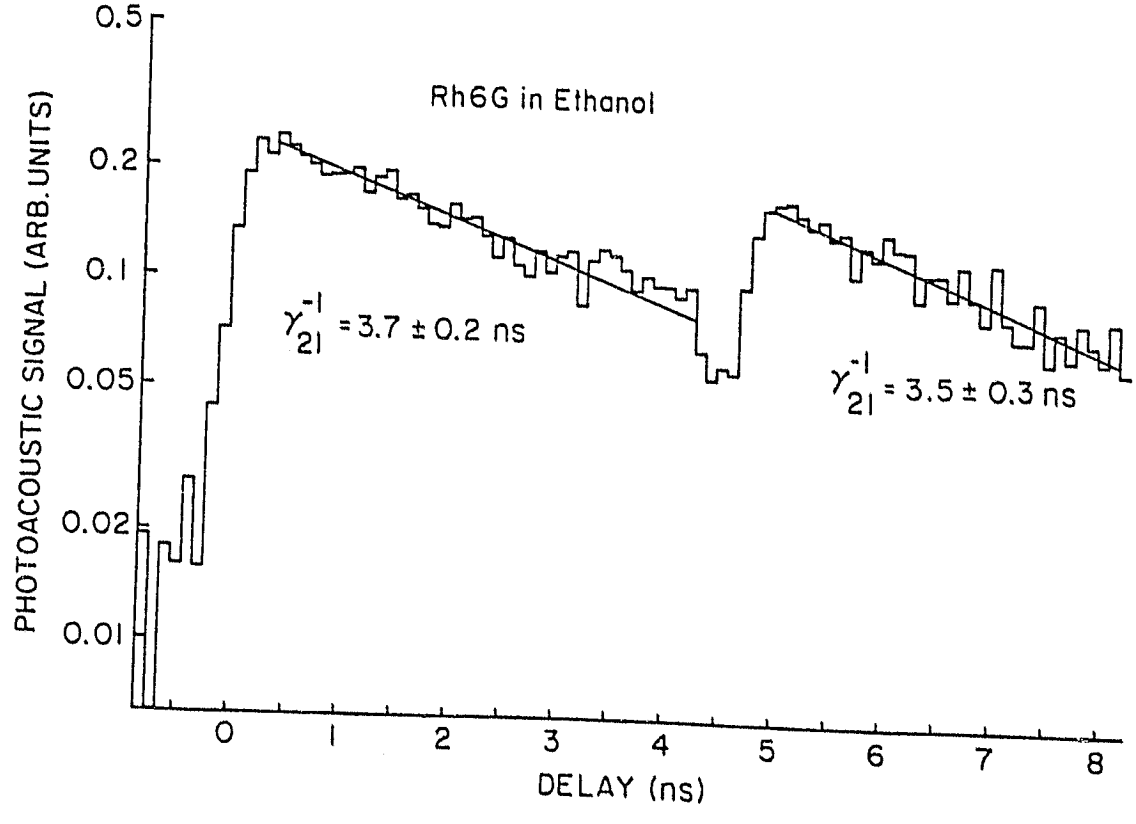

Figure 4

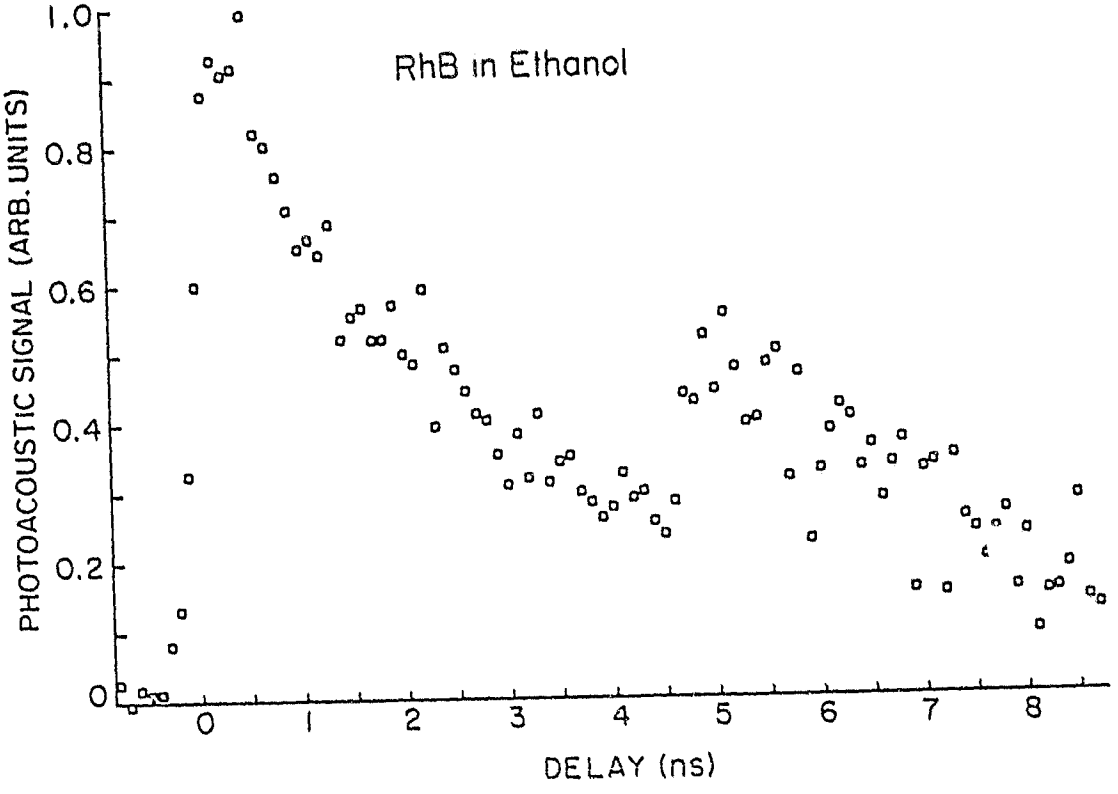

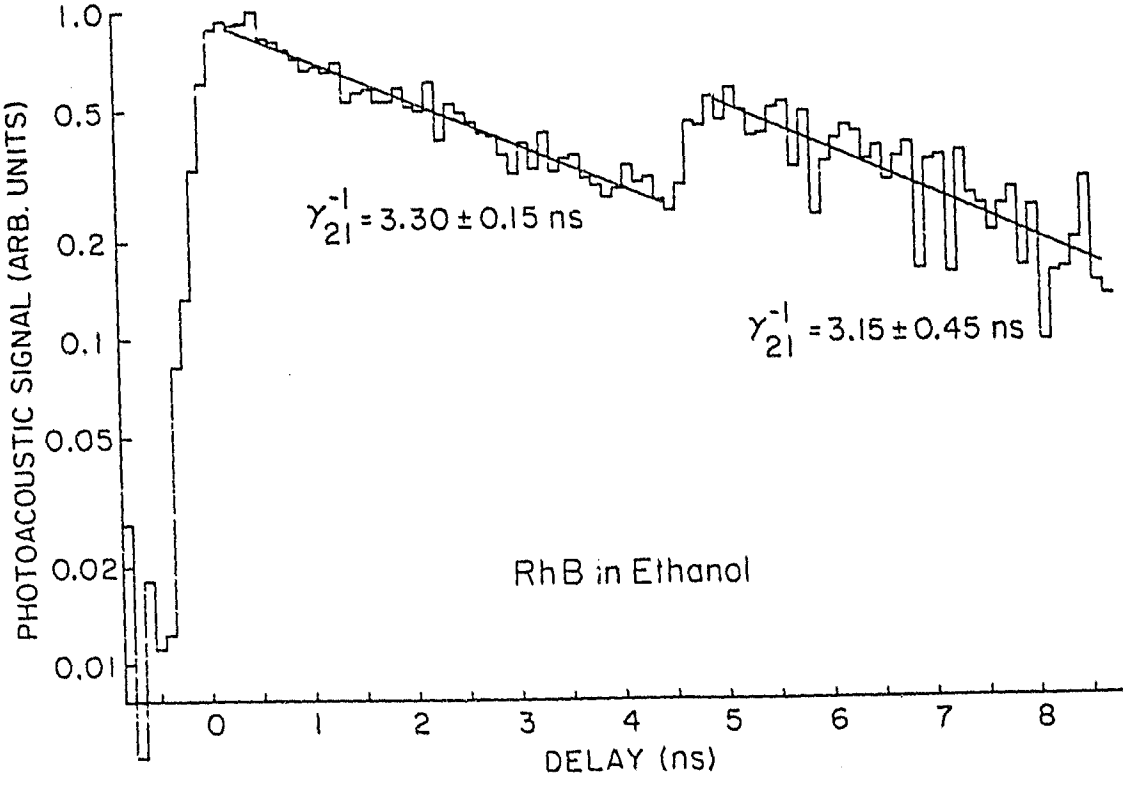

Figure 5

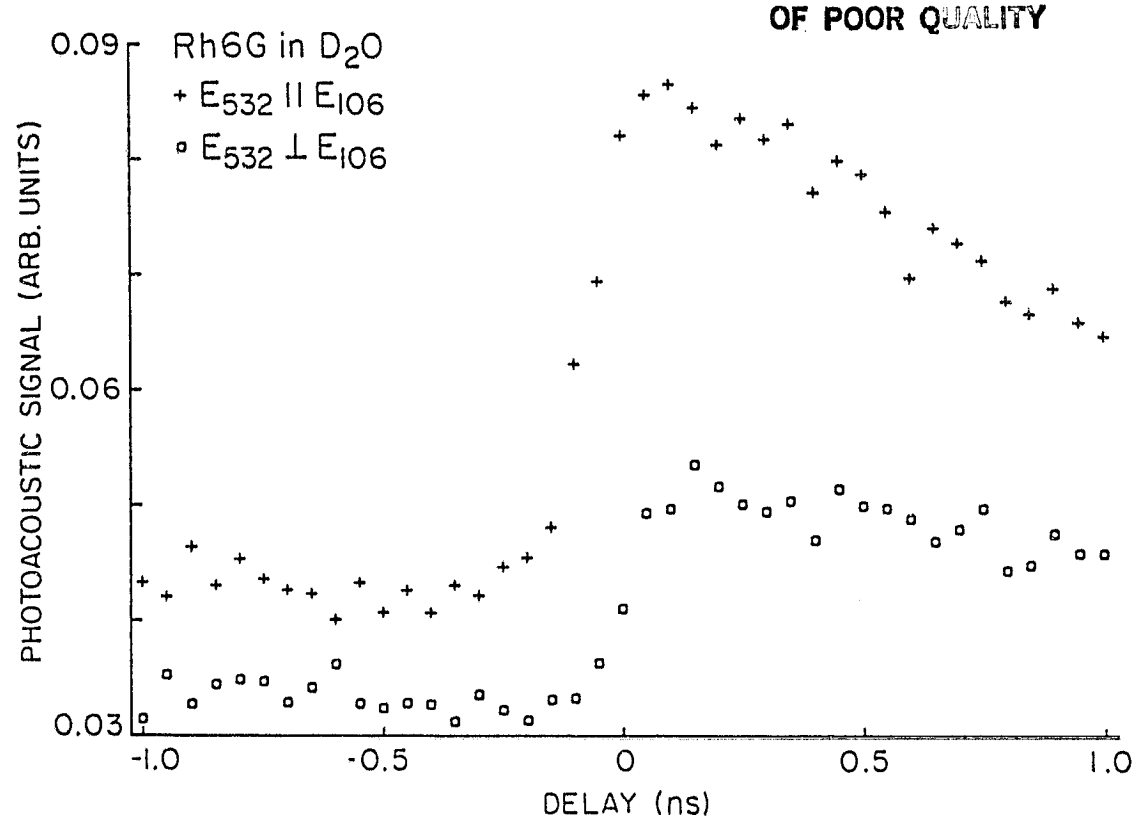

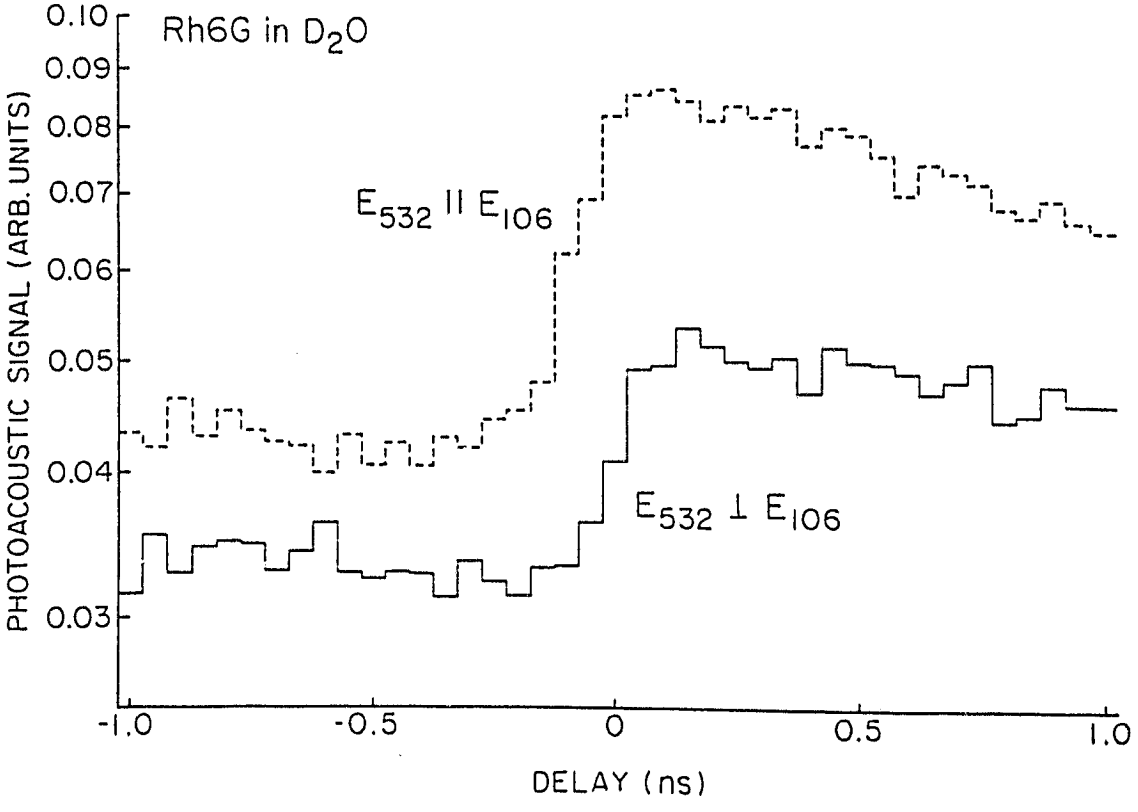

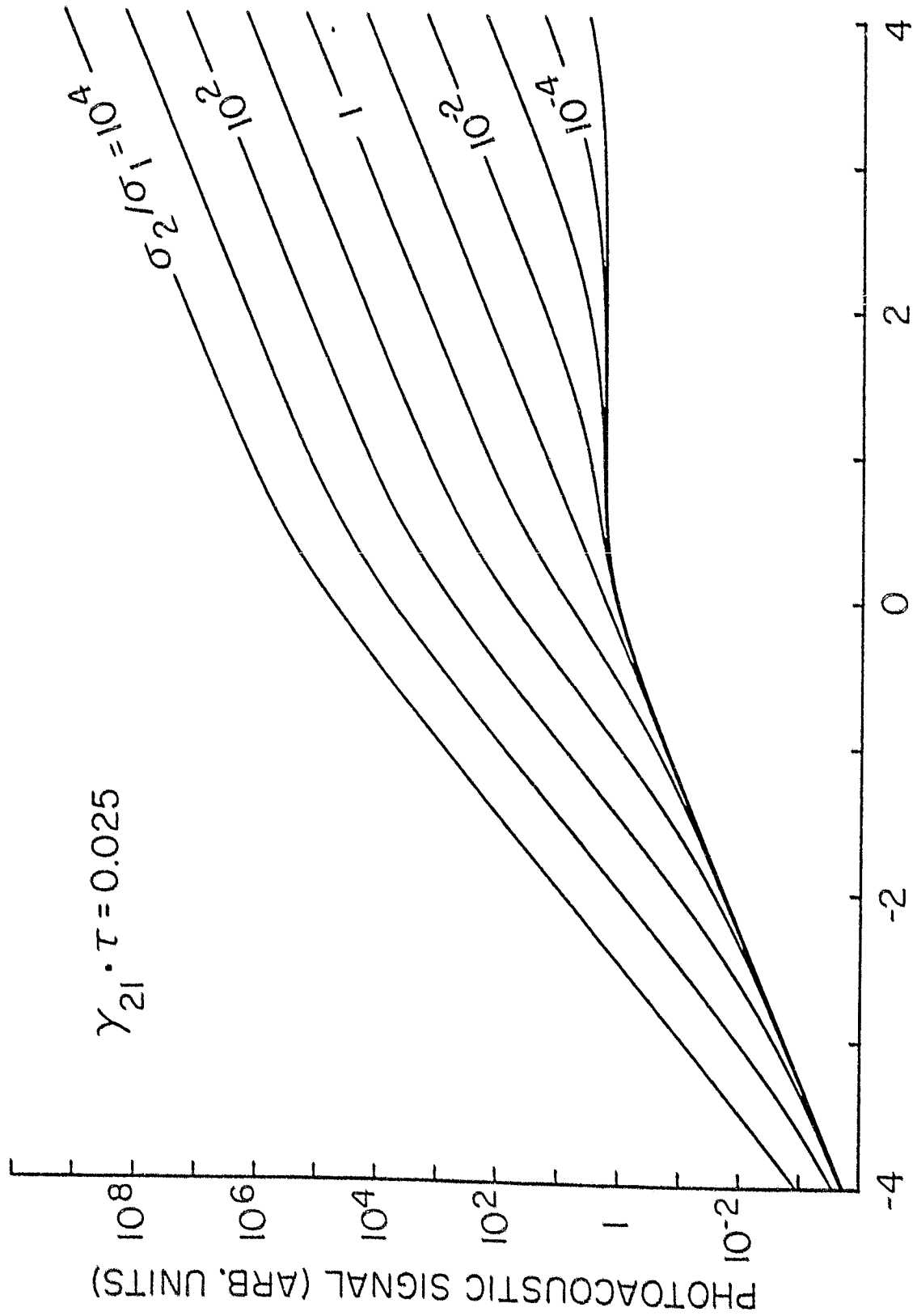

Figure 7

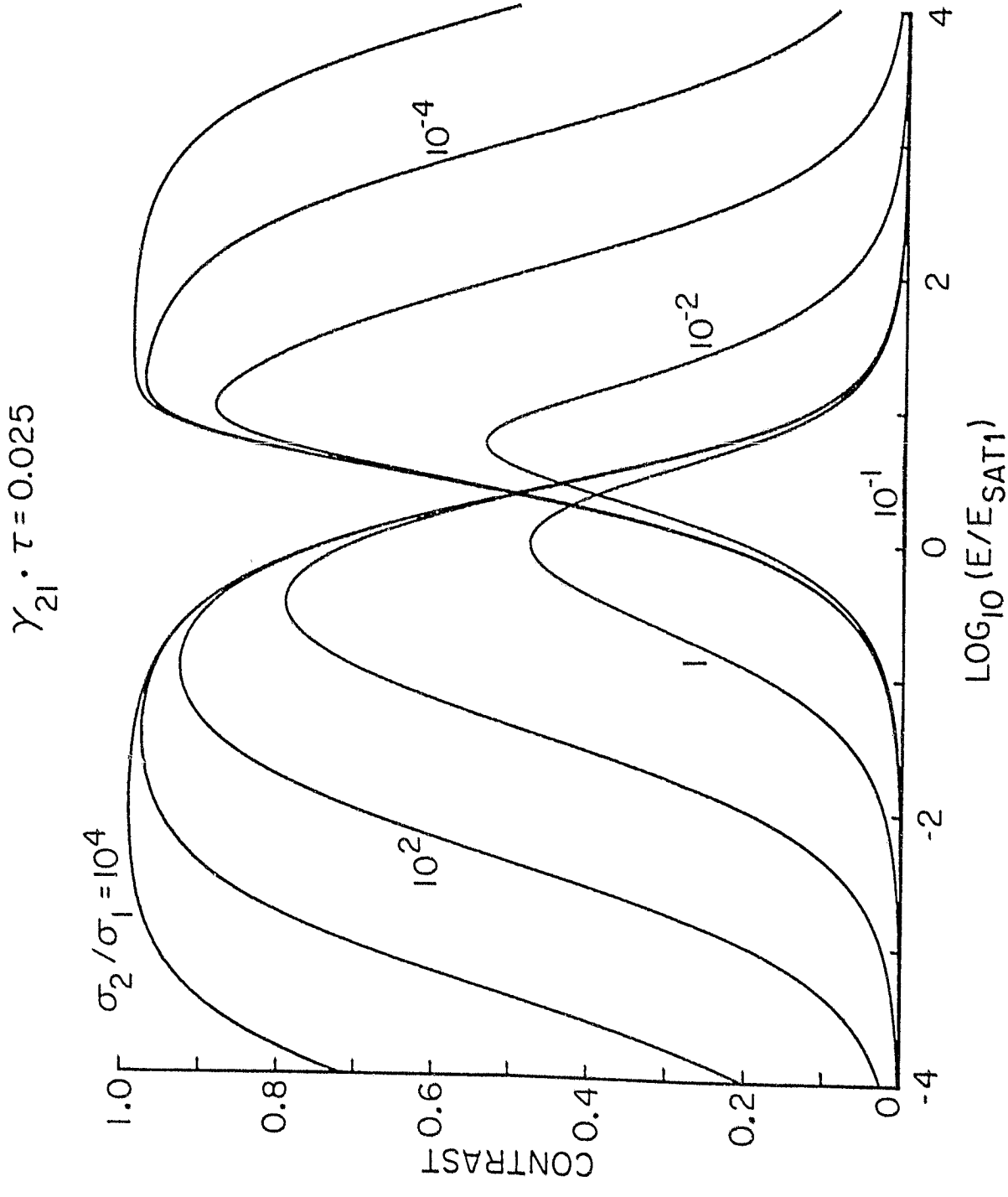

Figure 8

V. APPENDIX II

SPONTANEOUS RAMAN SCATTERING AS A HIGH RESOLUTION XUV RADIATION SOURCE

by

J.E. Rothenberg, J.F. Young, and S.E. Harris

Preprint

G.L. Report No. 3539

January 1983

supported by

Contract F49620-80-C-0023

and

NASA NAG 2-44

Edward L. Ginzton Laboratory
W.W. Hansen Laboratories of Physics
Stanford University
Stanford, CA 94305

SPONTANEOUS RAMAN SCATTERING AS A HIGH RESOLUTION XUV RADIATION SOURCE*

by

Joshua E. Rothenberg,† J. F. Young, and S. E. Harris
Edward L. Ginzton Laboratory
Stanford University
Stanford, California 94305

ABSTRACT

The paper describes a new type of high resolution XUV radiation source which is based upon spontaneous anti-Stokes scattering of tunable incident laser radiation from atoms excited to metastable levels. The theory of the source is summarized and two sets of experiments using He $(1s2s)^1S$ atoms, produced in a cw hollow cathode and in a pulsed high power microwave discharge, are discussed. The radiation source is used to examine transitions originating from the $3p^6$ shell of potassium. The observed features include four previously unreported absorption lines and several sharp interferences of closely spaced autoionizing lines. A source linewidth of about 1.9 cm^{-1} at 185,000 cm^{-1} is demonstrated.

---

*The work described here was supported by the Air Force Office of Scientific Research, the Army Research Office, and the National Aeronautics and Space Administration.

†Present address: IBM Watson Research Center, P.O. Box 218, Yorktown Heights, New York 10598.

SPONTANEOUS RAMAN SCATTERING AS A HIGH RESOLUTION XUV RADIATION SOURCE

by

Joshua E. Rothenberg, J. F. Young, and S. E. Harris
Edward L. Ginzton Laboratory
Stanford University
Stanford, California 94305

I. INTRODUCTION

Recent interest in extreme ultraviolet (XUV) physics has created a demand for extremely high resolution spectroscopic tools in this spectral region. Studies of autoionization and Rydberg series in atoms, as well as in molecular spectra, have shown important structure on the scale of 1 cm^{-1} [1].

To reach this resolution at 500 Å, where 1 Å is equivalent to 400 cm^{-1}, requires an instrumental linewidth of 2.5 mÅ, or a resolving power of 200,000. A 10-meter monochromator with an aberration free, 6000 ℓ/mm grating would attain this resolution at a slit width of 15 μm. The lack of availability of such instruments, along with the difficulties of low throughput and order sorting has made an alternative approach desirable. In this paper we report the development of a new radiation source in the XUV [2] and its application to high resolution spectroscopy [3,4].

The radiation source is based upon spontaneous Raman scattering [5,6] of incident laser photons from excited metastable atoms. The metastable atoms may be produced in a discharge; in this work both cw hollow cathode and high power pulsed microwave discharges are used. Metastable atoms may also be produced with a pulsed hollow cathode discharge [7] or, as recently demonstrated [8], by photoionization of ground level atoms by soft x-rays from a laser produced plasma.

The upper and lower sidebands of the scattered radiation have frequencies equal to the sum and difference, respectively, of the metastable storage frequency and the frequency of the incident laser photon. By tuning the frequency of the incident laser, the frequency of the scattered radiation is tuned. Each sideband has a linewidth equal to the convolution of the incident laser linewidth and the Doppler width of the radiating atoms. The accessible spectral range is therefore determined by the range of available tunable lasers, and by the number of species which may be used for metastable storage.

The spontaneous Raman radiation is only generated while the pump laser is present. Hence, the source may operate in a short pulse mode, and even on a picosecond time scale. If the storage and terminal states of the Raman process have zero angular momentum, and the pump laser is polarized, then the spontaneous Raman radiation will also be polarized.

In the following sections of this paper we first discuss the theory of the spontaneous Raman scattering source. Attention is given to intensity and saturation effects which limit its brightness. We then describe experimental work which, although limited to helium as the storage species, demonstrates the source as narrowband (resolution greater than 100,000 at 550 Å) and broadly tunable (spectral range of about 7,500 cm^{-1}). The source is used to examine transitions originating from the $3p^6$ shell of potassium. The observed features include four previously unreported narrow absorption lines and several sharp interferences of closely spaced autoionizing lines.

Finally, we consider the possibility of using the other inert gases, and also singly ionized column I metals for metastable storage. These species may allow a coverage of about 75% of the spectral region from 500 Å to 1500 Å.

II. THEORY

A. LINEAR SCATTERING CROSS SECTION

Figure 1 shows a partial energy level diagram of He. Energy is assumed to be stored in the He 1s2s ^{1}S metastable level at 20.6 eV. The initial level $|i\rangle$, is connected to the ground He $1s^2$ ^{1}S level $|f\rangle$ through a sum of intermediate levels $|n\rangle$ which have dipole allowed transitions to both the initial and final levels.

If a monochromatic pump field at frequency ω_p is applied to the system, the spontaneous Raman scattering of photons from metastable atoms can be visualized as a transfer of population to virtual levels at energies $\hbar(\omega_{if} \pm \omega_p)$ followed by spontaneous decay of this virtual population to the ground level $|f\rangle$. The process may be considered from either the point of view of an induced Einstein A coefficient, or of a linear scattering cross section. If N is the density (atoms/cm^3) of metastable storage atoms, then the number of XUV photons per sec which are scattered from a cm^3 of volume is

$$XUV_{photons/sec} = NA_{induced} = \frac{N\sigma_{spont}(P/A)_{pump}}{\hbar\omega_p} \qquad (1)$$

For laser pump intensities which are sufficiently low that saturation effects are not present, the differential scattering cross section for the upper sideband is given by

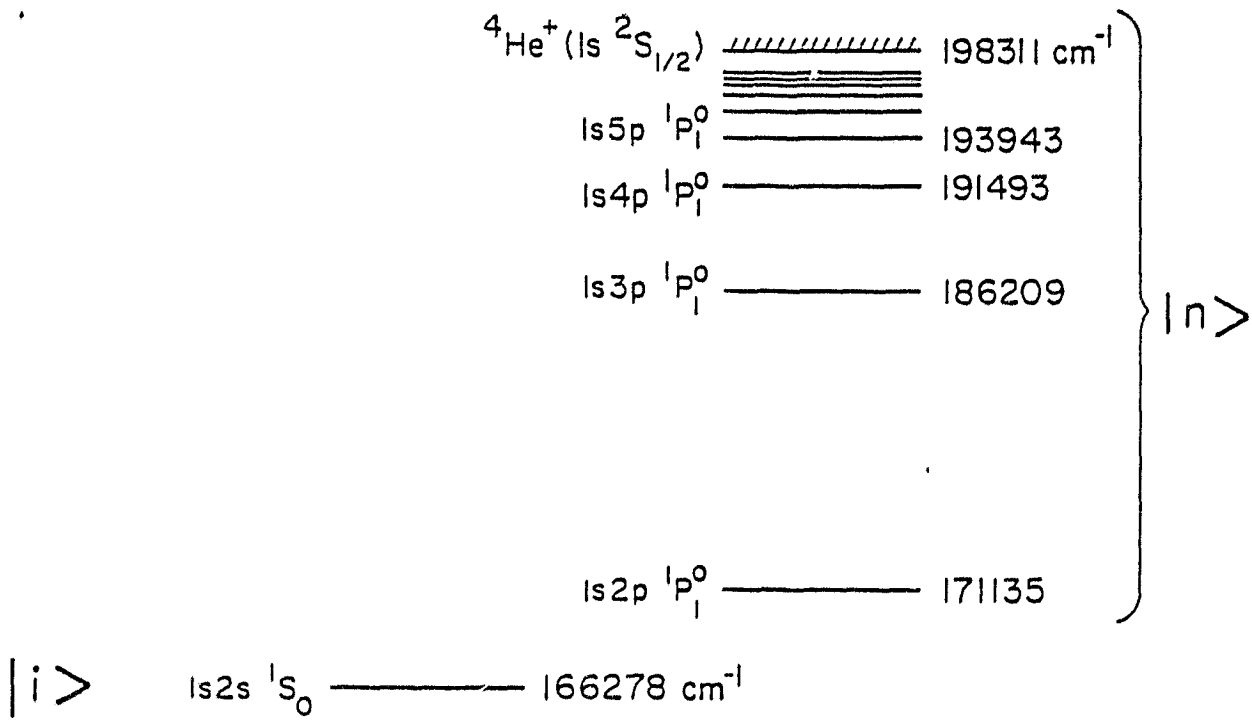

4838-11

Fig. 1--Atomic energy level diagram of ^4He.

$$\frac{d\sigma_{spont}}{d\Omega} = \frac{1}{16\pi^2}\,\frac{\omega_s^3\omega_p}{c^4\epsilon_0^2}\left|\sum_n \frac{\langle f|\vec{Q}\cdot\vec{\epsilon}_s^{\,*}|n\rangle\langle n|\vec{Q}\cdot\vec{\epsilon}_p|i\rangle}{E_n - E_f - \hbar\omega_s}\right.$$

$$\left. + \frac{\langle f|\vec{Q}\cdot\vec{\epsilon}_p|n\rangle\langle n|\vec{Q}\cdot\vec{\epsilon}_s^{\,*}|i\rangle}{E_n - E_i + \hbar\omega_s}\right|^2 \qquad (2)$$

where ω_s is the frequency of the scattered radiation ($\hbar\omega_s = E_i - E_f \pm \hbar\omega_p$), ω_p is the frequency of the pump photon, $\vec{\epsilon}_s$ and $\vec{\epsilon}_p$ are the respective polarization unit vectors, $\vec{Q} = -e\Sigma\vec{r}_i$ is the dipole moment operator for the atom, and E_i, E_n, and E_f are the energies of the initial, intermediate, and final states. The sum over intermediate states is performed over all dipole allowed transitions including the continua. To obtain the cross section for the lower sideband, simply replace $\vec{\epsilon}_p$ by $\vec{\epsilon}_p^{\,*}$ in Eq. (2). In the case of He, the upper sideband will have smaller resonance denominators, and therefore a significantly larger scattering cross section than does the lower sideband.

Figure 2 shows the upper sideband (anti-Stokes) scattering cross section [9] for He where the initial state is the metastable singlet level He 1s2s ^{1}S, the final state is the ground level, and the intermediate levels are $|n\rangle$ = 1snp ^{1}P and the 1sep ^{1}P continuum. The resonances are due to the intermediate levels 1s2p ^{1}P at 584 Å and 1s3p ^{1}P at 537 Å. As a result of both the ω_s^3 dependence of the scattering, and also of the relatively close approach to resonance, the per atom anti-Stokes scattering cross section in the XUV is often about six orders of magnitude larger than is typically encountered in the visible region of the spectrum.

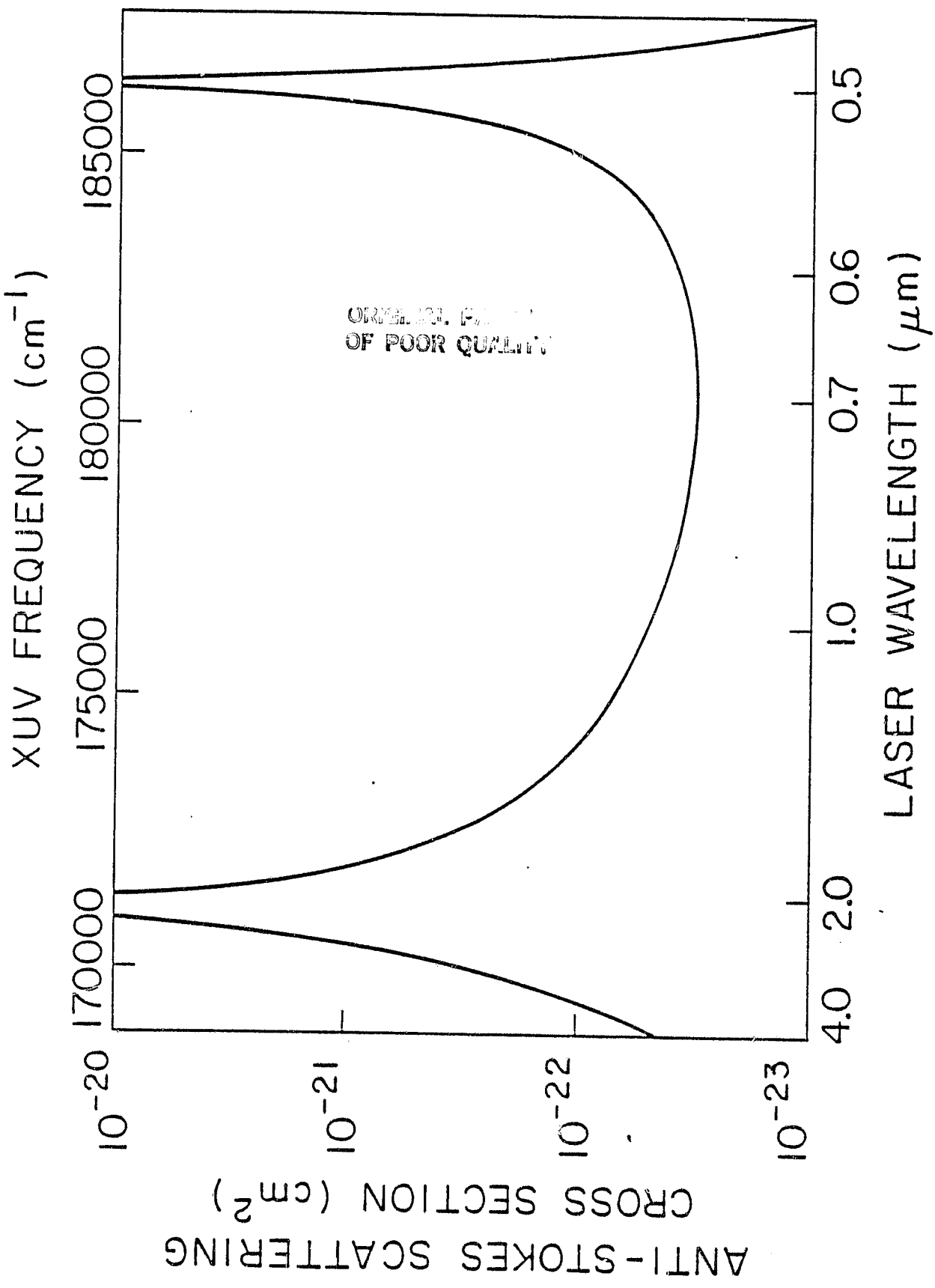

Fig. 2--Plot of anti-Stokes scattering cross section vs. tunable laser wavelength and scattered XUV frequency.

B. SATURATION

Three types of saturation of the anti-Stokes radiation source are typically encountered. These are: (1) simple depletion of the stored metastable population, (2) microscopic (per atom) saturation of the scattering process, and (3) macroscopic saturation, in the Planck equilibrium sense, of the emitting media.

1. Depletion

If we assume, as almost always will be the case, that the stored metastable population is not so large that the Raman scattering process represents a significant loss to the incident laser beam, then the laser pulse energy fluence which in essence scatters or depletes all of the stored population is

$$(J/A)_{saturation} = \frac{\hbar\omega_p}{\sigma_s} \qquad (3)$$

For a typical scattering cross section in He of $\sigma_s = 5 \times 10^{-23}$ cm^2, and ω_p corresponding to 6000 Å, this occurs at $J/A = 6.6 \times 10^3$ joules/cm^2. For beam size of several mm^2, as will most often be used in the spectroscopic applications of this source, this type of saturation is unlikely to be encountered.

2. Microscopic Saturation

As the incident laser power is raised, or a particular intermediate resonance is approached, all of the atoms in the storage level are in effect transferred to the virtual level and may then not radiate or scatter at a rate faster than the Einstein A coefficient of the approached intermediate

level. As this large field, or near resonance region, is approached, frequency shifts of the storage level and therefore of the scattered Raman radiation also occur, and may limit the resolution of the radiation source.

A simple and nearly exact solution of the near resonant problem is obtained from the dressed atom approach [10]. Defining the quantity θ by

$$\theta = \tan^{-1}\left(\frac{\mu_{in}E_p}{\hbar\Delta\omega}\right) \tag{4}$$

where μ_{in} and $\Delta\omega$ are the matrix element and detuning from the near resonant level $[\Delta\omega = \omega_n - (\omega_i + \omega_p)]$; the induced emission rate is

$$A_{induced} = \left(\frac{\omega_s}{\omega_{nf}}\right)^3 \sin^2\frac{\theta}{2} A_{nf} \tag{5}$$

and the frequency of the scattered anti-Stokes radiation is

$$\omega_s = (\omega_i - \omega_f) + \omega_p - \frac{\delta}{2} \tag{6a}$$

where

$$\delta = \Delta\omega\left(\frac{1 - \cos\theta}{\cos\theta}\right) \tag{6b}$$

When θ is small (low pump fields or large detunings), Eq. (5) reduces to a single term of Eq. (2).

3. Macroscopic Saturation

In a typical discharge or plasma the population of the final level (in He, the ground level) of the Raman process is often several orders of magnitude greater than the population of the metastable storage level. Incident

laser photons not only cause emission of XUV photons from the storage level, but also cause two-photon absorption of these same photons by atoms which are in the ground level. The interplay of the two-photon emission, i.e., the Raman emission, and the two-photon absorption yield a source brightness which is the same as that of a one-photon blackbody, except that the usual one-photon absorption coefficient is replaced by the two-photon absorption coefficient [2].

The brightness $B(\omega)$ (power per bandwidth in radians/sec per solid angle and area) for a sample of thickness L, is given by

$$B(\omega) = \frac{\hbar\omega^3}{8\pi^3 c^2}\left[\frac{1}{(N_f/N_i) - 1}\right]\left[1 - e^{-(N_f - N_i)\sigma^{(2)}(\omega)L}\right] \tag{7a}$$

$$\sigma^{(2)}(\omega) = \frac{8\pi^3 c^2}{\omega^2}\,\frac{d\sigma_{spont}}{d\Omega}\,\frac{(P/A)_{pump}}{\hbar\omega_p}\,g(\omega) \tag{7b}$$

where $\sigma^{(2)}$ is the two-photon absorption cross section for XUV radiation which results from the presence of the laser field ω_p. The lineshape $g(\omega)$ is the convolution of the initial (metastable) and final level lineshapes.

At frequencies or cell lengths where the column is two-photon opaque, the brightness of the spontaneous Raman radiation source is that of a blackbody at a Boltzmann temperature of the metastable level, i.e., $N_i/N_f = \exp[-(\hbar\omega_{if}/kT)]$. In the optically thin region where $N_f\sigma^{(2)}L \ll 1$, the brightness reduces to that obtained from the linear scattering cross section of Eq. (2).

III. EXPERIMENTAL RESULTS

A series of experiments was performed to demonstrate the use of spontaneous Raman scattering as a tunable high resolution source for absorption spectroscopy. The metastable helium $1s2s\ ^1S$ level was used as the Raman medium, producing radiation in the 500 Å spectral region (anti-Stokes upper sideband scattering). We used this source to examine potassium absorption features due to autoionizing transitions originating from the $3p^6$ shell. Two methods were used to excite helium atoms to the $1s2s\ ^1S$ storage level: a cw hollow cathode discharge and a high power pulsed microwave discharge. The first technique produced anti-Stokes radiation which was brighter than all other XUV emission from the plasma, thus simplifying detection; however, the radiation was relatively weak, thus limiting the tuning range. The second technique produced much larger anti-Stokes signals and greater tuning ranges, but the increased level of background XUV plasma emission made the use of additional filtering necessary. Both methods are described below.

A. LOW CURRENT HOLLOW CATHODE DISCHARGE

A schematic of the basic apparatus is shown in Fig. 3. Helium metastable $1s2s\ ^1S$ population was produced in a 60 cm long hollow cathode discharge and a tunable dye laser (Nd:YAG pumped Quanta-Ray PDL-1) was directed down the discharge by a right-angle turning prism. Backward scattered anti-Stokes radiation passed by the prism (which obscured about one-half the aperture), through a potassium vapor cell, through an aluminum filter, and was incident on an electron multiplier tube.

The discharge consisted of a stainless steel cylindrical cathode 1.2 cm in diameter inside a concentric 2.5 cm stainless steel tube which served as

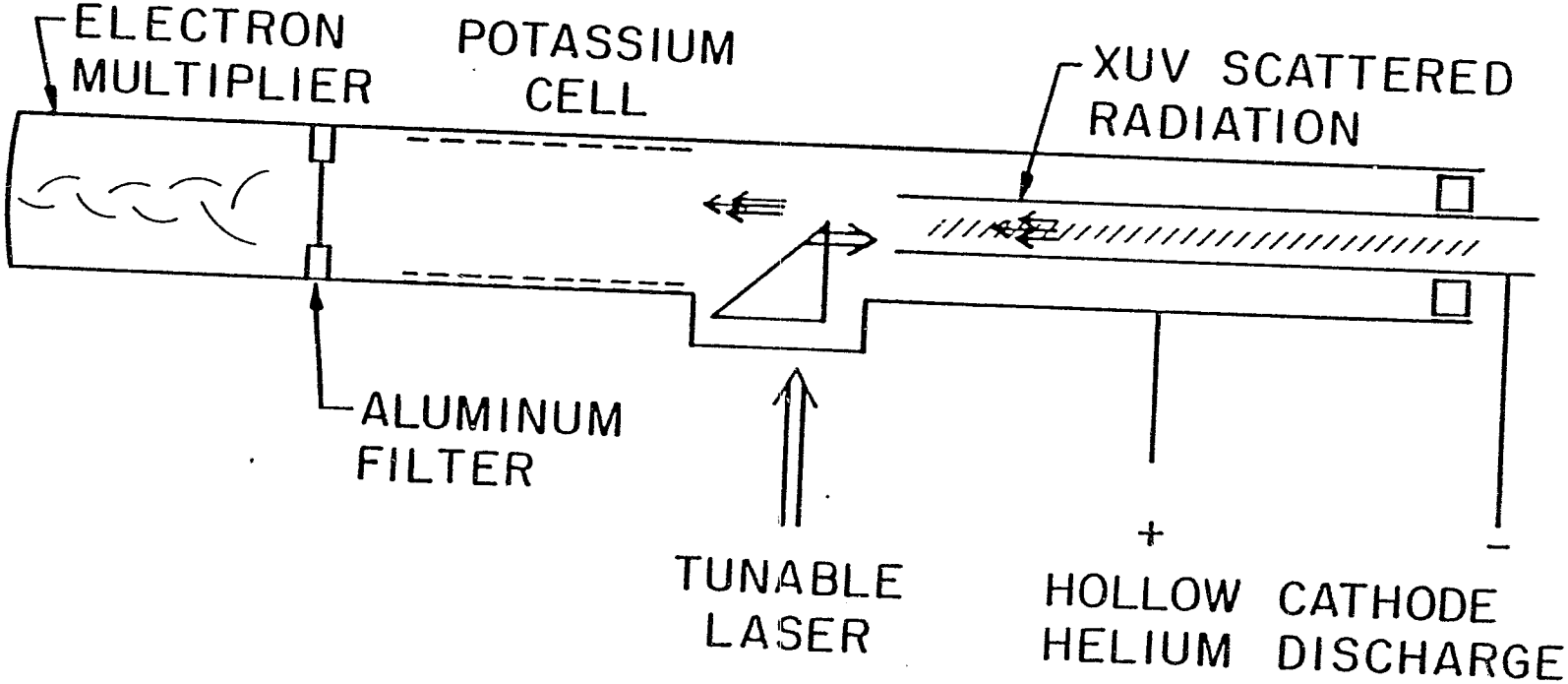

Fig. 3--Schematic of hollow cathode apparatus used for absorption spectroscopy of potassium.

the anode. The cathode had a slot 0.6 cm wide along the 60 cm active length of the discharge which allowed the glow to reside inside the cathode. Typical operating parameters of the discharge were 2 torr helium, 190 V, and 30 ma, which, based on previous measurements [11], implies a population of $1s2s\ ^1S$ metastables of about 10^{11} atoms/cm^3. The current through the discharge was kept low because it was found that the metastable population did not increase appreciably with current (up to a few hundred ma), but the background radiation from the plasma (predominantly resonance line radiation at 584 Å and 537 Å) increased linearly with the applied current. Thus, the largest signal-to-noise ratio was obtained at the lowest stable operating current of the discharge.

The potassium vapor cell consisted of a stainless steel tube 1.2 cm in diameter with a stainless steel wick. The active hot zone was 5 cm long and typically was operated at a potassium vapor density of 10^{15} atoms/cm^3 (260°C). The ambient helium discharge pressure slowed the diffusion of potassium both into the discharge and to the aluminum filter which served to separate the 2 torr helium pressure from the 10^{-6} torr operating pressure of the electron multiplier. Experiments were performed with potassium having a minimum purity of 98% and 99.95% with the same results.

The XUV photons transmitted through the potassium cell impinged directly upon the first dynode of an EMI D233 electron multiplier, liberating photoelectrons which were subsequently amplified in the remaining 13 stages of the tube. This fast linear focused tube provided single output pulse widths of ~ 5 ns and a gain of ~ 10^6 at an applied voltage of 3.7 kV. The output of the electron multiplier was processed with a fast preamplifier and a 10 ns wide gated integrator. A small computer digitized and recorded the resultant

voltage along with the input dye laser intensity. The computer also tuned the laser in steps of 0.048 Å.

For incident laser pulses of 50 mJ at 6000 Å we calculate that about 4.3×10^{7} XUV photons per laser pulse are produced in the 60 cm long discharge at the anti-Stokes wavelength, 540.6 Å. The solid angle of the detector reduces the flux to 200 photons/pulse or (for the 10 pulse per second repetition rate) 2000 photons/sec. Thus, the ratio of the number of incident laser photons to the number of effective XUV photons is expected to be greater than 10^{14}. It is therefore essential to provide large discrimination against the visible laser photons. This was accomplished (1) by using a geometry which utilized backscattered XUV radiation, (2) by the $\sim 5 \times 10^{-8}$ rejection of the visible light by the aluminum filter, and (3) by the high work function of the electron multiplier. Even with these factors, if the incident laser reflected off an edge near the end of the discharge, the reflection overwhelmed the detected XUV photons. The transmittance of the aluminum filter (Luxel TF-101a, a 1500 Å thick film of Al alloyed with 1% silicon supported by a nickel mesh) is useful from ~ 850 Å to ~ 150 Å. At 550 Å approximately 10% of the incident flux is transmitted, whereas in the visible the filter is specified at less than 5×10^{-8} transmittance [12]. Therefore, we estimate the incident flux onto the detector at 200 photons/sec; assuming a detector quantum efficiency of 10% [13], we obtain a count rate of 20 counts/sec, which agrees well with our observations.

The spectral regions studied with this apparatus are shown in Table 1. Typical absorption scans are shown in Fig. 4. These scans are computer generated plots in which each point represents the sum of integrated signals from 5 laser settings, a total of 50 pulses covering ~ 0.75 cm^{-1}. The XUV

Table 1

Spectral Regions Studied with the

Hollow Cathode Discharge

Laser Dye	Range of Laser Wavelength (Å)	Range of XUV Frequency (cm^{-1})
Kiton Red 620	5990 – 5740	182975 – 183695
Rhodamine 590	5760 – 5470	183635 – 184549
Coumarin 500	5220 – 4880	185435 – 186769

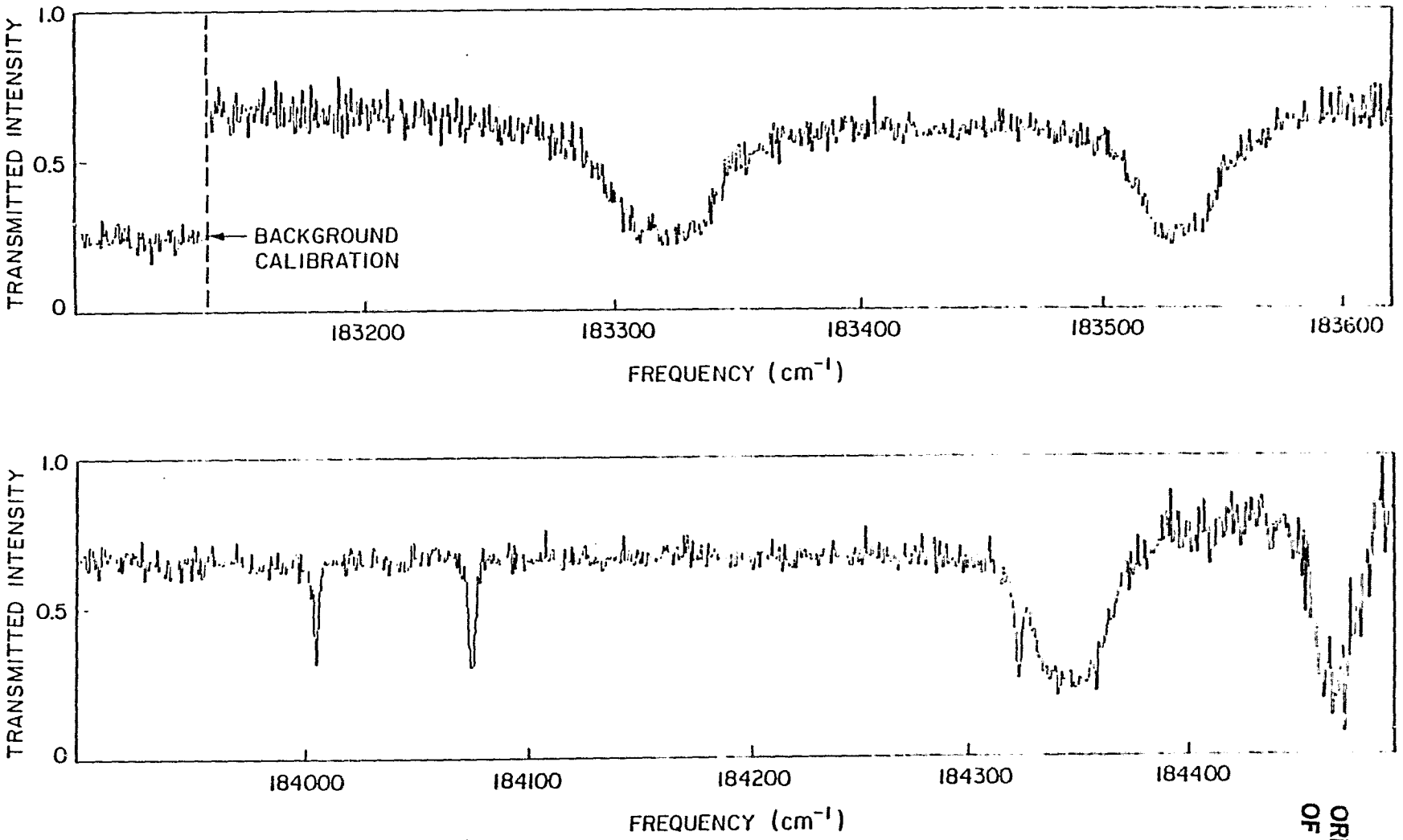

Fig. 4--Absorption scans of potassium obtained with hollow cathode apparatus. Potassium vapor density is 10^{15} atoms/cm^3, and cell length is 5.0 cm.

signal was normalized to the relative dye laser intensity, which has the effect of increasing the statistical fluctuation in regions of lower laser intensity.

The XUV frequency at each data point was obtained by adding the laser frequency to the frequency of the storage level, ^{4}He 1s2s ^{1}S, which has been accurately measured to be 166,277.55 ± 0.15 cm^{-1} [14,15]. The laser frequency was determined from the dial of the Quanta-Ray dye laser; this dial reading was calibrated using known Ne and Kr lines, and found to be resettable to ± 1 cm^{-1}.

Table 2 summarizes the energies and linewidths of the observed potassium absorption features. The broader features were observed by Mansfield [16], Mansfield and Ottley [17], and Kavei, et al. [18]. The narrower features have not been reported previously. We estimate that Mansfield [16] had an instrumental linewidth of approximately 40 cm^{-1} based upon microdensitometer traces he supplied. Thus, it is not surprising that weak lines a few cm^{-1} in width would escape detection. (Assuming that the linewidths of these features are about equal to that of the anti-Stokes radiation, a 50% absorption in Fig. 4 corresponds to an oscillator strength of $f = 3 \times 10^{-4}$.)

Our measured absorption linewidths were a function of the potassium vapor pressure, and the widths reported in Table 2 are the minimum full widths at half maximum obtained by reducing the cell pressure to a value at which negligible change in width was seen with further reduction. The narrowest observed absorption feature (at 185,806 cm^{-1}) had a measured width of 1.9 cm^{-1}, which approaches the theoretical linewidth of the anti-Stokes radiation, i.e., the convolution of the 0.3 cm^{-1} laser linewidth and the room temperature Doppler width of ~ 1.3 cm^{-1} of the emitting helium atoms [19].

Table 2

Potassium Absorption Features Observed with the Hollow Cathode Apparatus

Energy	Linewidth	Designation	Previously Observed Energy
183320 ± 1 cm^{-1}	8.4 cm^{-1}	$3p^5 3d(^3P)5s\ ^2P_{1/2}$	183322 (a) cm^{-1}
183530	10.5	$3p^5 3d(^3P)5s\ ^2P_{3/2}$	183532 (a)
184008	2.6		
184076	3.4		184076 (b)
184321	2.5		
184344	15.0	$3p^5 4s(^1P)5s\ ^2P_{3/2}$	184342 (a)
184465	7.8	$3p^5 4d(^3P)5s\ ^2P_{1/2}$	184471 (a)
185806	1.9		
186659	5.0	$3p^5 4d(^1D)4s\ ^2D_{3/2}$	186656 (a)

(a) M. W. D. Mansfield (1975) [Ref. 16].
(b) G. Kavei, et al. (1977) [Ref. 18].

Note that potassium vapor (at 260°C) has a Doppler width of ~ 0.5 cm^{-1} in this spectral region. A calculation which convolves the various linewidths involved shows that an observed 1.9 cm^{-1} linewidth implies a natural width of the line of ~ 0.5 cm^{-1}. This corresponds to an autoionizing time of ~ 10 ps, which is consistent with calculated autoionizing times for levels in potassium which are not allowed to autoionize to first order (in LS coupling) [20]. Thus, the narrow absorption lines are probably the result of transitions from the $3p^6 4s$ ground level to levels that, in the approximation of LS coupling, are forbidden by selection rules to autoionize, such as odd parity doublet series levels with even orbital angular momentum and levels in the quartet series.

As a result of the operation of the discharge at very low current, this apparatus had the inherent disadvantage of producing low signal levels. For a total of 50 pulses integrated per data point, we found that a dye laser energy of ~ 12 mJ/pulse was necessary to achieve an acceptable 3 to 1 signal-to-noise ratio. The spectral range that could be scanned in a reasonable time period (the scans shown in Fig. 4 took ~ 1-1/2 hours each to complete) was therefore limited to wavelengths generated using tunable radiation from the high output laser dyes. Thus, in order to investigate other spectral regions the inherent anti-Stokes signal level must be increased.

B. PULSED HIGH POWER MICROWAVE DISCHARGE

We made two changes to increase the brightness and thus the tuning range of the anti-Stokes radiation source: a high power microwave discharge was used to produce a larger population in the He 1s2s ^1S storage level, and the effective solid angle for collection of anti-Stokes radiation was improved.

The basic geometry is similar to that used previously and is shown in Fig. 5. Microwave pulses at 9.375 GHz, 2 μs long, with a peak power of about 500 kW were generated by a Varian SFD-303 coaxial magnetron and coupled into a 90 cm long, 4 mm i.d. quartz tube located inside a section of x-band waveguide, centered adjacent to the narrow wall. Helium gas at ~ 5 torr was flowed slowly through the tube. The helium broke down regularly during the rising edge of the microwave pulse; approximately 60% of the incident microwave energy was absorbed and less than 5% was reflected. Previous measurements [21] of microwave excited helium plasmas indicate that 1s2s ^{1}S storage level densities of about 10^{13} atoms/cm^3 are typically obtained, or about 100 times larger than achieved with the hollow cathode.

In addition, this apparatus collected a much larger fraction of the generated anti-Stokes radiation by making use of near-grazing incidence reflections of the XUV radiation at the inside surface of the quartz tube. At 500 Å, quartz reflects 90% of radiation incident at 88° [22], and the tube acts like a waveguide for these grazing rays. As illustrated in Table 3, the effective solid angle collection of such a tube can be larger by a factor of 10^2 - 10^3 than a similar geometry where there is no reflection of grazing rays. The second column of Table 3 shows the solid angle collected from a uniformly emitting source through a quartz tube of inside diameter 4 mm assuming no wall reflections, i.e., as if the tube were replaced by apertures at its ends. The third column shows the solid angle collected for the same geometry, except that the reflections are included. We note, however, that these reflections depolarize the initially polarized anti-Stokes radiation.

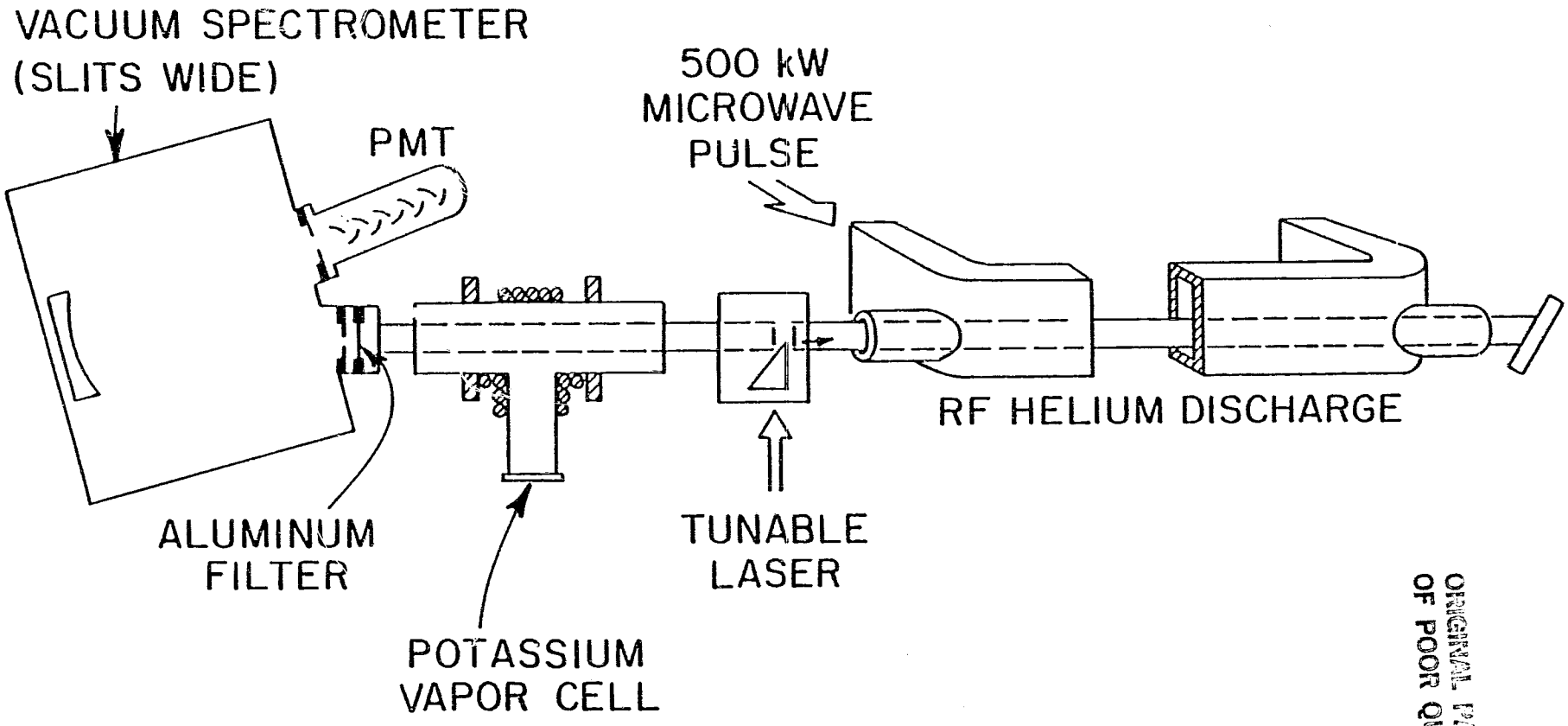

Fig. 5--Schematic of microwave pumped apparatus used for absorption spectroscopy of potassium.

Table 3

Collected Solid Angle Through a 4 mm Diameter Quartz Tube

Uniformly Illuminated at One End

Tube Length (cm)	Solid Angle Without Reflections (Steradians)	Solid Angle Including Reflections (Steradians)
10	1.2×10^{-3}	0.035
20	3.1×10^{-4}	0.019
50	5.0×10^{-5}	8.2×10^{-3}
100	1.2×10^{-5}	4.3×10^{-3}
200	3.1×10^{-6}	2.2×10^{-3}
400	7.8×10^{-7}	1.1×10^{-3}

The potassium vapor cell (Fig. 6) was redesigned so as to maintain the grazing reflection geometry. An alkali resistant glass tube was slotted (1 mm wide) to allow potassium vapor to permeate throughout, and a heater was wound on the glass tube to keep it hotter than the wet stainless steel wick, so as to prevent potassium condensation inside the tube. The potassium cell had an active hot zone 4.5 cm long. Over approximately 30 hours of operation, the potassium cell's throughput of XUV radiation decreased by a factor of 5. Apparently, this was due to contamination of and/or reactions on the inside surface of the glass tube, and a subsequent loss of reflectivity, since the throughput returned to its original value when the contaminated tube was replaced.

The main disadvantage in using the more intense microwave discharge was that the intensity of the spurious XUV radiation was much larger than the anti-Stokes signal intensity. The 584 Å integrated resonance line intensity was measured to be 15 times greater than the anti-Stokes intensity (using 50 mJ of laser energy at 6000 Å). As a result, it was necessary to filter the resonance radiation from the anti-Stokes radiation. A McPherson 225 one-meter normal incidence vacuum monochromator with a 1200 ℓ/mm grating ruled over a 30 mm × 50 mm area and coated with platinum was used in first order as a filter against the resonance radiation. The linear dispersion was 8.3 Å/mm, and the monochromator slit widths were set to discriminate against the nearest noise feature, while passing the desired range of anti-Stokes radiation. For the spectral range that we examined, the nearest noise feature was the second resonance line at 537.0 Å. Typically, the slits were set at a width of 0.8 - 1.0 mm, and thus, the resolution of the apparatus was due entirely to the spectral width of the anti-Stokes radiation.

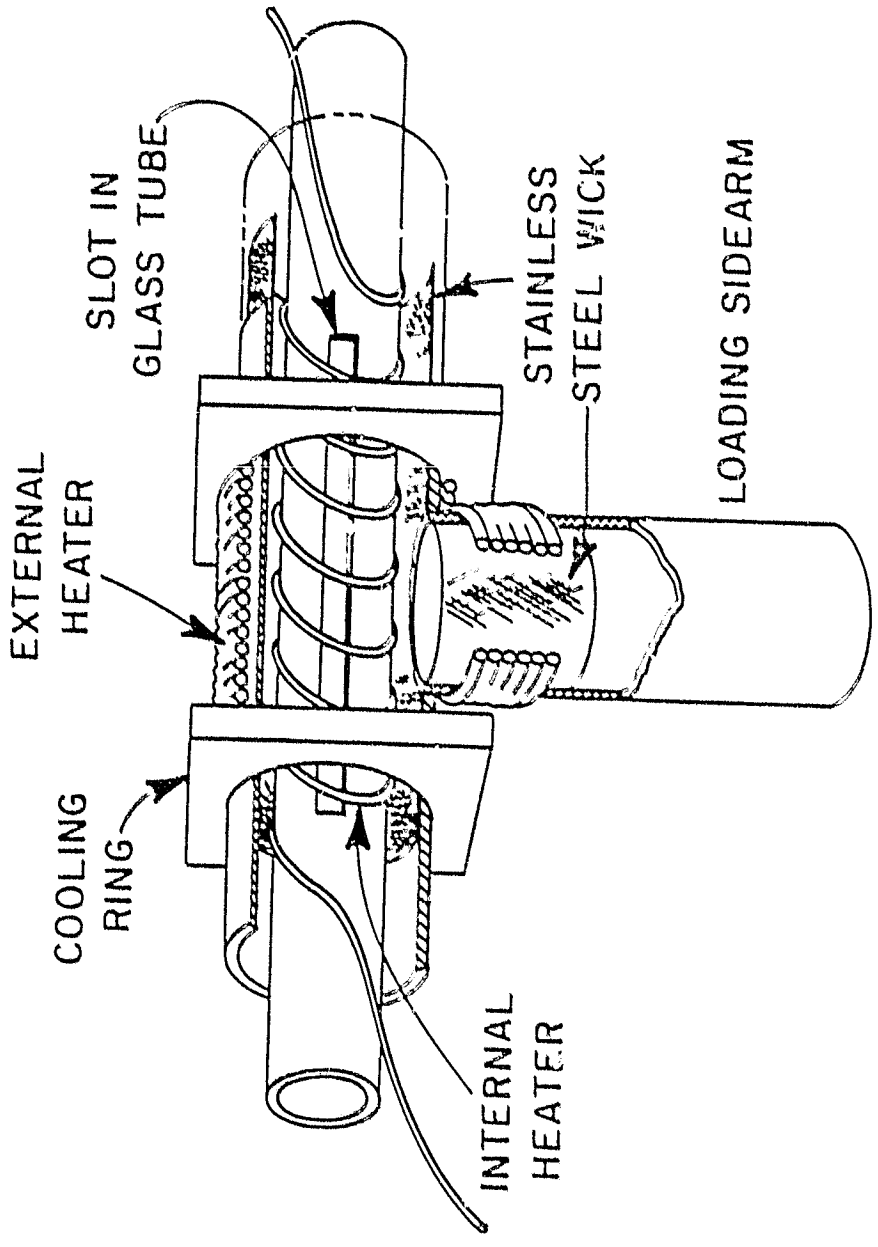

Fig. 6--Potassium vapor cell used with microwave apparatus.

The spectrometer, however, introduced a large throughput loss into the system. For an incident pulse energy of 25 mJ at 6000 Å through the helium plasma, we calculate that approximately 3.2×10^9 anti-Stokes photons are generated. Of these photons scattered into all directions, only an estimated 0.029%, or 9.3×10^5 photons emerge from the end of the potassium absorption cell. (Without the grazing-reflection collection this output would have been smaller by roughly 200.) Furthermore, the solid angle of the spectrometer reduces the collected flux by an additional factor of 15, the grating has an efficiency in the XUV of about 4%, and the aluminum filter transmits 10% of the anti-Stokes radiation. Thus, we estimate that about 250 photons strike the detector for each laser pulse. At ten laser pulses per second, this implies a flux of 2.5×10^3 photons/sec striking the detector, or for a 10% detector quantum efficiency, a net count rate of 250 per second. The observed count rate was ~ 200/sec, 10 times greater than with the hollow cathode.

The temporal behavior of the microwave excited discharge is shown in Fig. 7. The anti-Stokes radiation and resonance fluorescence intensities are proportional to their respective excited state populations. Thus, we conclude that in the first few hundred ns after breakdown (the avalanche period), the excited state populations reached their maximum value. For the duration of the microwave pulse, resonance fluorescence remained large, but the anti-Stokes radiation decreased to a small level. After the microwave pulse, recombination occurred in the cooling plasma, and both anti-Stokes radiation and resonance fluorescence regained intensity. The anti-Stokes radiation decayed during recombination with a time constant of ~ 4 μs, whereas resonance fluorescence decayed with a shorter time constant of

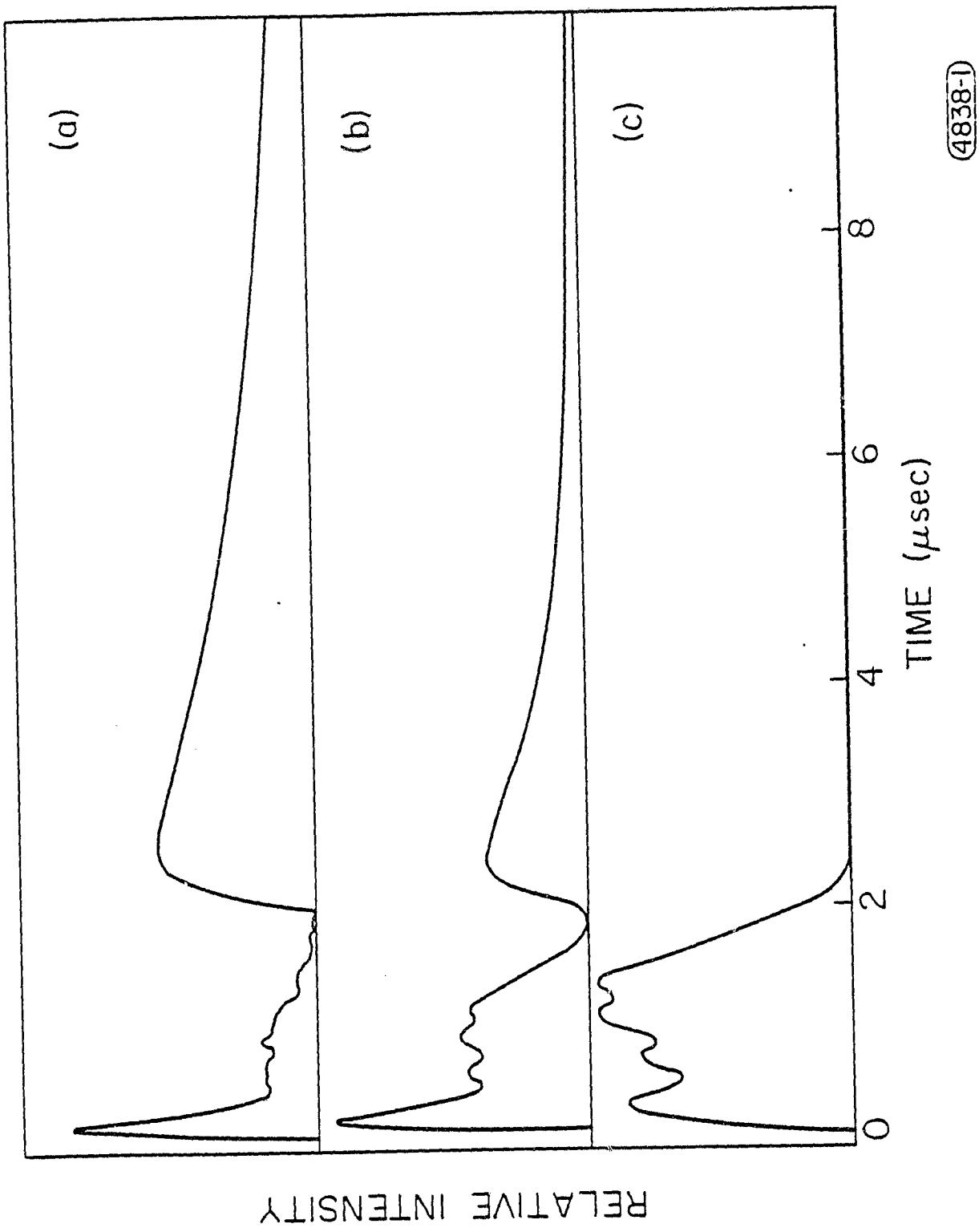

Fig. 7--Temporal behavior of microwave discharge emission. (a) Anti-Stokes output at 550 Å, (b) resonance line emission at 584 Å, and (c) input microwave pulse.

~ 2 μs. Thus, the ratio of anti-Stokes intensity to resonance line intensity was largest in this recombination tail.

Unfortunately, operation late in the recombination period has a serious disadvantage. The measured widths of absorption features in potassium were about 2.5 cm^{-1} wider than measurements of the same features made during the avalanche period. We believe that this is due to an increase in the temperature of the metastables and hence, a larger Doppler width during the recombination period. The most likely mechanism for this heating is the elastic collisions of neutrals and ions with hot electrons, and the subsequent formation of hot metastables during the recombination period. From linewidth measurements during the recombination period we estimate that the Doppler width is 3.5 cm^{-1}, which implies an atomic kinetic temperature of ~ 3000°K (0.26 eV). The spectral width of the anti-Stokes radiation during the avalanche period was confirmed to be equal to that obtained with the hollow cathode discharge by measuring the linewidths of the same potassium absorption features. Because of this effect, all the measurements and spectra reported were made during the avalanche period.

Using the microwave discharge we extended the spectral region examined in potassium to 536.8 Å - 558.4 Å, as shown in Table 4. To achieve a signal-to-noise ratio of 3 to 1 with an integration of 50 laser pulses per point, a minimum of ~ 1 mJ of laser energy per pulse was required. Commercial sources of such energy per pulse are available to at least 2 μm, which implies a possible XUV spectral range of ~ 537 Å - 584 Å.

Table 5 lists a number of additional potassium absorption features we observed using the microwave excited discharge; all have been previously observed by Mansfield [16]. Typical absorption scans are shown in Fig. 8, which are computer generated plots containing 1024 points corresponding to laser

Table 4

Spectral Regions Studied with Microwave Excited

Anti-Stokes Radiation Source

Laser Dye	Range of Laser Wavelength (Å)	Range of XUV Frequency (cm^{-1})
Rhodamine 640	5960 - 6140	183055 - 182654
Sulforhodamine 640	6090 - 6180	182697 - 182458
DCM	6170 - 6600	182484 - 181224
Pyridine 1	6680 - 7220	181247 - 180127
Styryl 7	7210 - 7510	180146 - 179592
Styryl 8	7500 - 7800	179610 - 179098

Table 5

Linewidths and Positions of Potassium Absorption Features

Observed with the Microwave Apparatus

Energy (cm^{-1})	Linewidth (cm^{-1})	Designation	Previously Observed Energy (cm^{-1})
179885	4.0	$3p^5 3d(^3D)4s\ ^2D^o_{3/2}$ [a]	179886 [a]
179918	2.1		179920
180547	43.0	$3p^5 3d(^1P)4s\ ^2P^o_{1/2}$	180551
180794	55.0 [b]	$3p^5 3d(^1P)4s\ ^2P^o_{3/2}$	180791
180840	11.0 [b]		180850
181519	2.7		181517
181745	5.5	$3p^5 3d5s\ ^4P^o_{3/2}$	181742
182152	8.8		182152
182652	5.6		182651

[a] Energies and designations from Mansfield [Ref. 16].

[b] Lines very asymmetric; linewidths determined from fit to theoretical Fano profile.

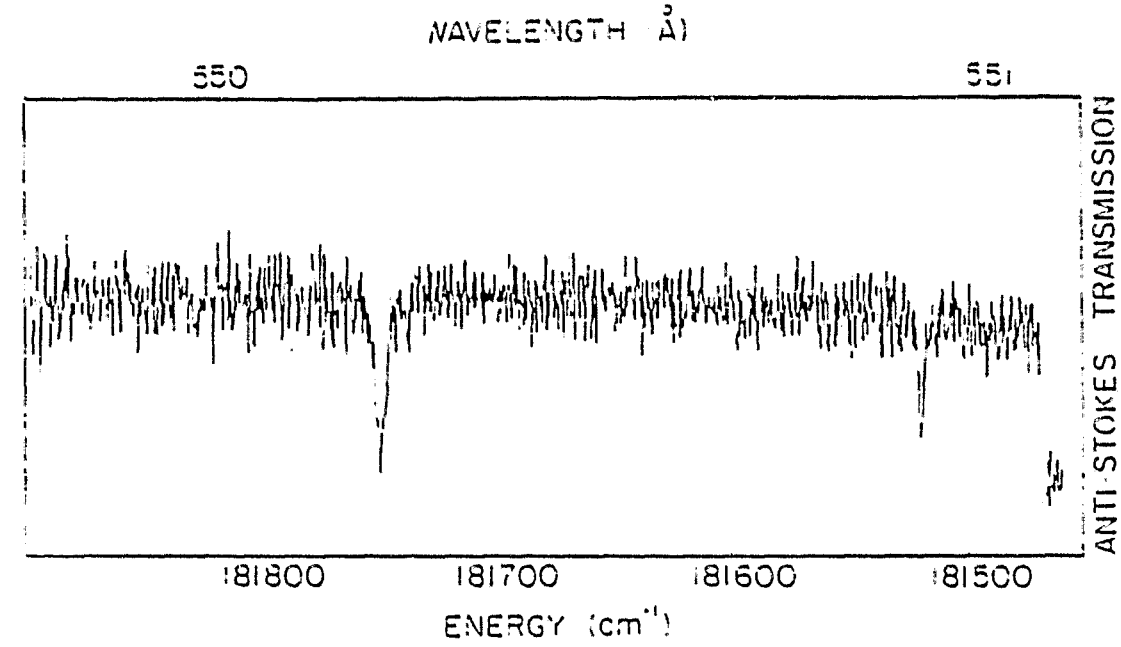

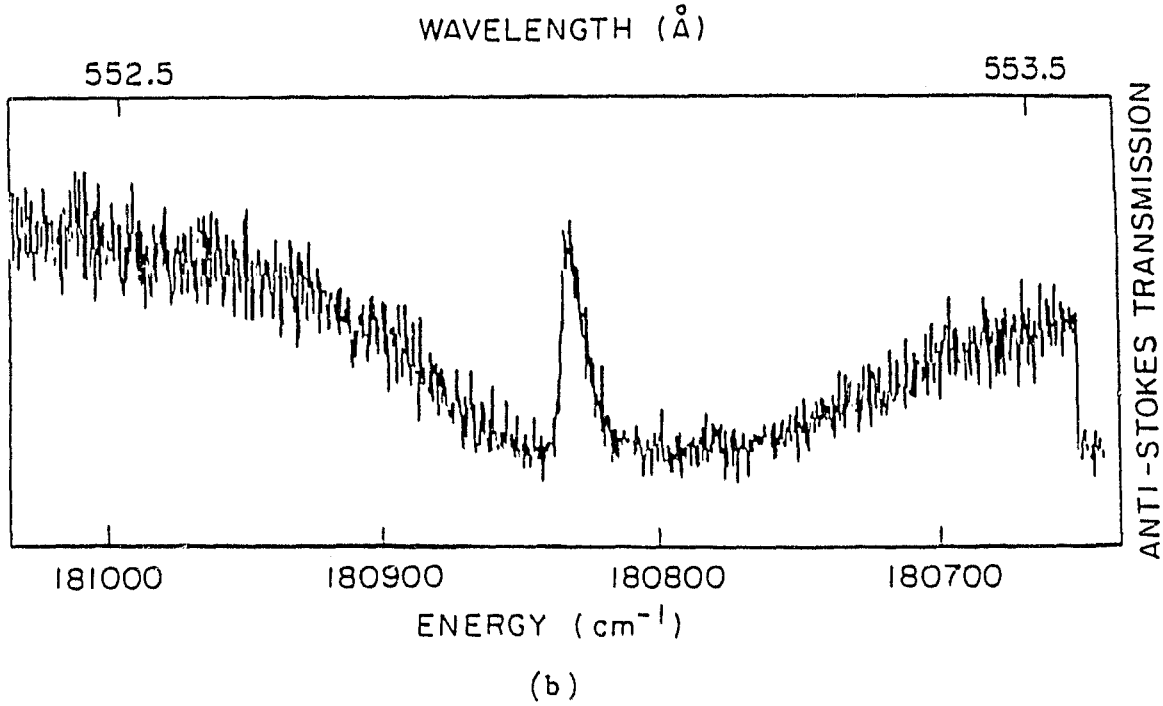

Fig. 8--Absorption scans of potassium obtained with microwave apparatus. Potassium cell length was 4.5 cm.
(a) Potassium vapor density was 1.0×10^{15} atoms/cm^3.
(b) Potassium vapor density was 2.2×10^{15} atoms/cm^3.

wavelength settings separated by 0.18 Å. To reduce the effects of background drifts, the computer rapidly scanned the laser wavelength and recorded the collected XUV flux level at each laser wavelength setting. At the end of each scan the laser was blocked to determine the background level. The plots of Fig. 8 represent the sum of 50 such scans, each one having only one laser pulse at each laser wavelength setting. The 50 scans took about 1-1/2 hours to complete.

Figure 8(a) shows two fairly narrow features at 181745 cm^{-1} and 181519 cm^{-1}, while Fig. 8(b) shows two broad, asymmetric features centered at 180794 cm^{-1} and 180840 cm^{-1} separated by a narrow ~ 100% transmission window. (The transmission level at the right end of the scan is reduced by an additional feature at 180547 cm^{-1}, beyond the range of the displayed scan.) The two (somewhat saturated) absorption features in Fig. 8(b) have very asymmetric profiles due to a strong interference between two discrete levels lying nearby in a single continuum. A complete cancellation of absorption cross section between two levels can be explained in terms of a Beutler-Fano [23] profile, and a simple analysis yields the ratio of the absorption cross section to the underlying continuum cross section. The values of the linewidths given in Table 5 for these levels were obtained by fitting absorption data taken at lower density, shown in Fig. 9, to the theoretical results. The theoretical calculation is represented by the solid line.

Highly asymmetric features such as these are somewhat rare in this region of the potassium absorption spectrum because of the small background photoionization cross section [24]. The Fano lineshape parameter q for a single discrete state in a continuum is then very large (typically 30 - 50 in potassium), and hence, the lineshape function is quite symmetric. In the

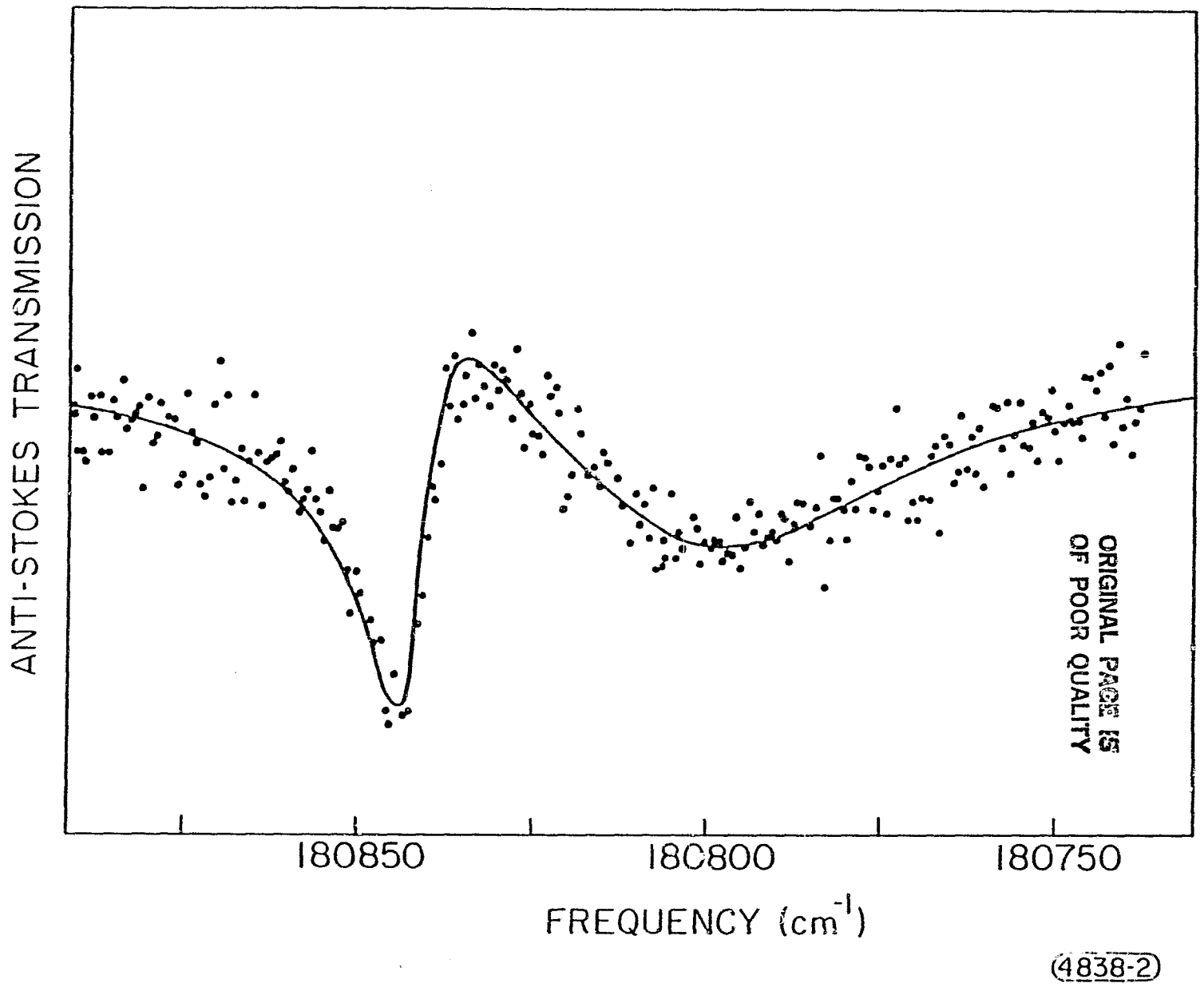

Fig. 9--Fit of theoretical Fano profile to potassium absorption data.

case discussed above, with two discrete states lying nearby, one can visualize the autoionization wing of one state as increasing the "background" photoionization cross section the other state sees. The q parameter of this state is thereby reduced, resulting in a very asymmetric lineshape. This intuitive approach is confirmed by the more exact result shown in Fig. 9.

IV. EXTENSION TO OTHER SYSTEMS

Using helium as the storage medium, the coverage of the spontaneous Raman anti-Stokes radiation source is limited by practical tunable lasers to the spectral region from approximately 537 Å to 584 Å. To access other spectral regions one must use different storage levels or other species.

Table 6 and Fig. 10 show how the other inert gases might be used to allow coverage of new spectral regions. In all of the inert gases, except for helium, the state of primary metastability has a total angular momentum of $J = 2$ and is also of opposite parity to that of the ground level [25]. In order to use these lowest metastable levels for anti-Stokes scattering one must therefore use a low power fixed frequency laser to resonantly transfer the population to a level of the same parity as ground and then use an intense tunable laser to generate the lower spontaneous Raman sideband. The $J = 1$ intermediate level will resonantly enhance the scattering cross section for this lower sideband.

Table 6 notes the primary storage level in each of the inert gases, the wavelength of the weak transfer laser, the center wavelength of the strong tunable laser, and the center wavelength of the emitted XUV radiation. The final column of this table notes the Doppler width for each of the species at 300°K.

Table 7 shows how the alkali ions might be used in an iso-electronic analogy to the noble atoms in Table 6. The Na II system which is iso-electronic to neon is shown in Fig. 11. We note that spontaneous anti-Stokes scattering in Li II has been observed by Willison, et al. [26].

One difference in using the iso-electronic column I ion is that the primary storage level may be populated by creating a core shell hole by

Table 6

Spontaneous Raman Scattering in the Inert Gases

Element	Metastable Level	Weak Transfer Laser Wavelength (Å)	Center Tunable Laser Wavelength (Å)	Center XUV Wavelength (Å)	Doppler Width (cm^{-1}) at 300°K
He	$1s2s\ ^1S$	--	5015 20581	537 584	1.15 1.06
Ne	$2p^5(^2P^o_{3/2})3s_{J=2}$	5944	6680	736	0.375
Ar	$3p^5(^2P^o_{3/2})4s_{J=2}$	7067	8408	1048	0.187
Kr	$4p^5(^2P^o_{3/2})5s_{J=2}$	5564	8266	1165	0.116
Xe	$5p^5(^2P^o_{3/2})6s_{J=2}$	4526 9048	8349 9926	1296 1470	0.0835 0.0736

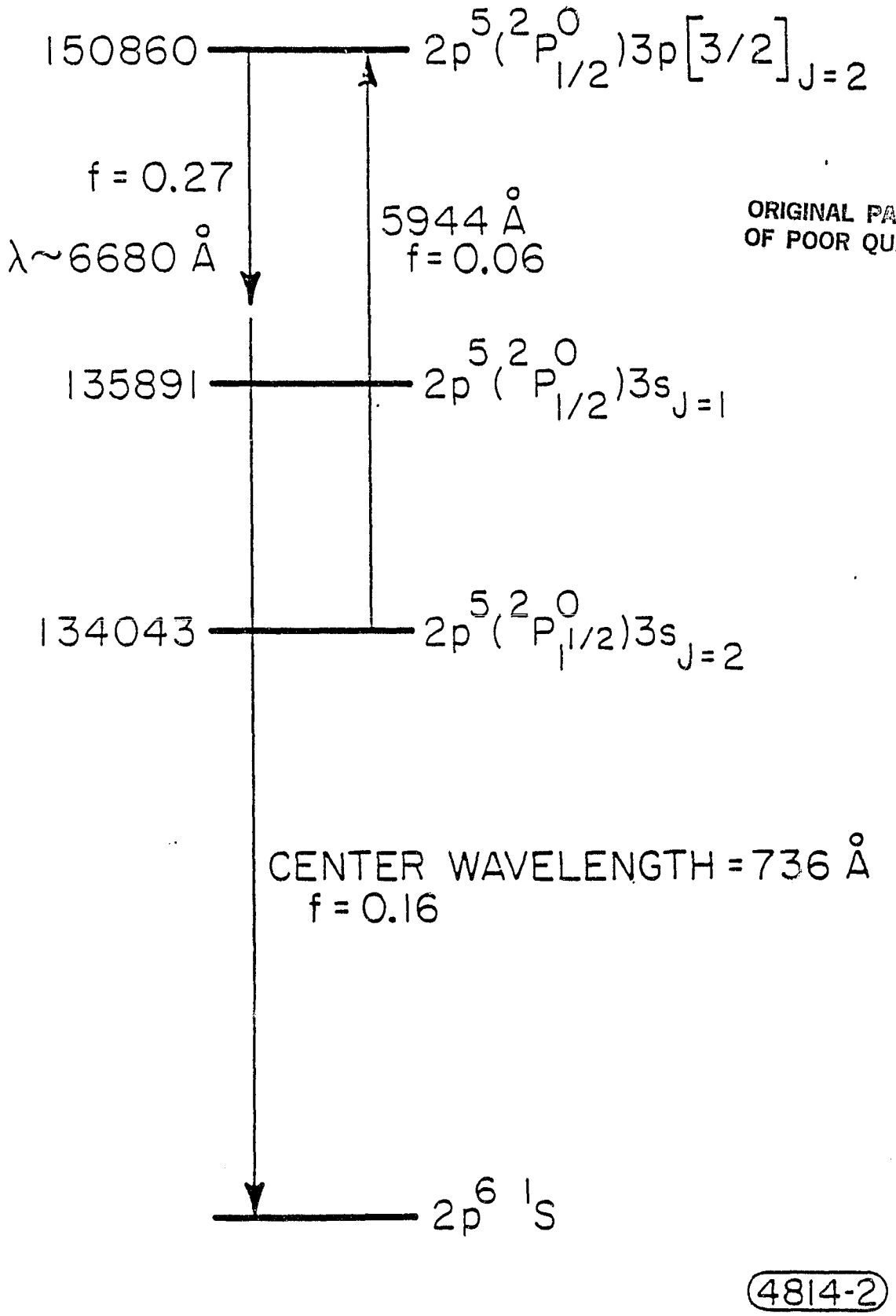

Fig. 10--Atomic energy level diagram showing spontaneous Raman scattering in neon.

Table 7

Spontaneous Raman Scattering in the Alkali Ions

Element	Metastable Level	Weak Transfer Laser Wavelength (Å)	Center Tunable Laser Wavelength (Å)	Center XUV Wavelength (Å)	Doppler Width (cm^{-1})	Temperature (^oK)
Li II	$1s2s\ ^1S$	--	9584	199	4.6	1150
Na II	$2p^5(^2P^o_{3/2})3s_{J=2}$	2843	3191	372	1.13	800
K II	$3p^5(^2P^o_{3/2})4s_{J=2}$	3683	4310	601	0.504	700
Rb II	$4p^5(^2P^o_{3/2})5s_{J=2}$	3162	4650	697	0.283	650
Cs II	$5p^5(^2P^o_{3/2})6s_{J=2}$	2778 4832	4871 4954	814 927	0.187 0.164	600

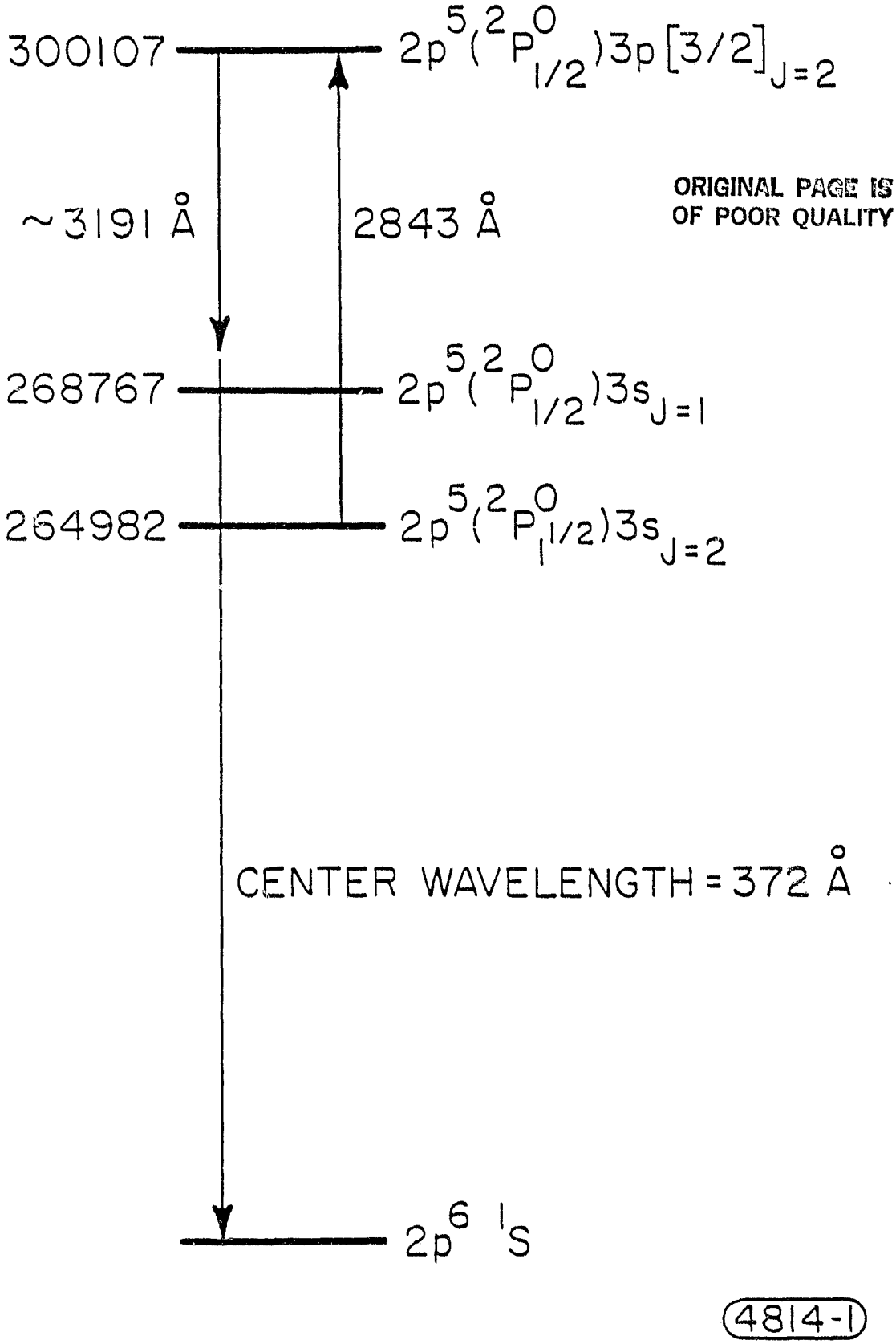

Fig. 11--Atomic energy level diagram showing spontaneous Raman scattering in Na^+.

photoionization. In recent experiments, Caro, et al. [8] have used photoionization to produce populations as large as 3×10^{15} ions/cm^3 in the helium-like Li^+ triplet metastables.

If we assume that a frequency interval of 10,000 cm^{-1} can be attained with each of the Raman systems listed in Tables 6 and 7, then the total spectral range accessible to the anti-Stokes radiation source would be that shown in Fig. 12. This represents approximately 25% of the frequency interval from 200 Å to 1500 Å and approximately 75% of the interval from 500 Å to 1500 Å.

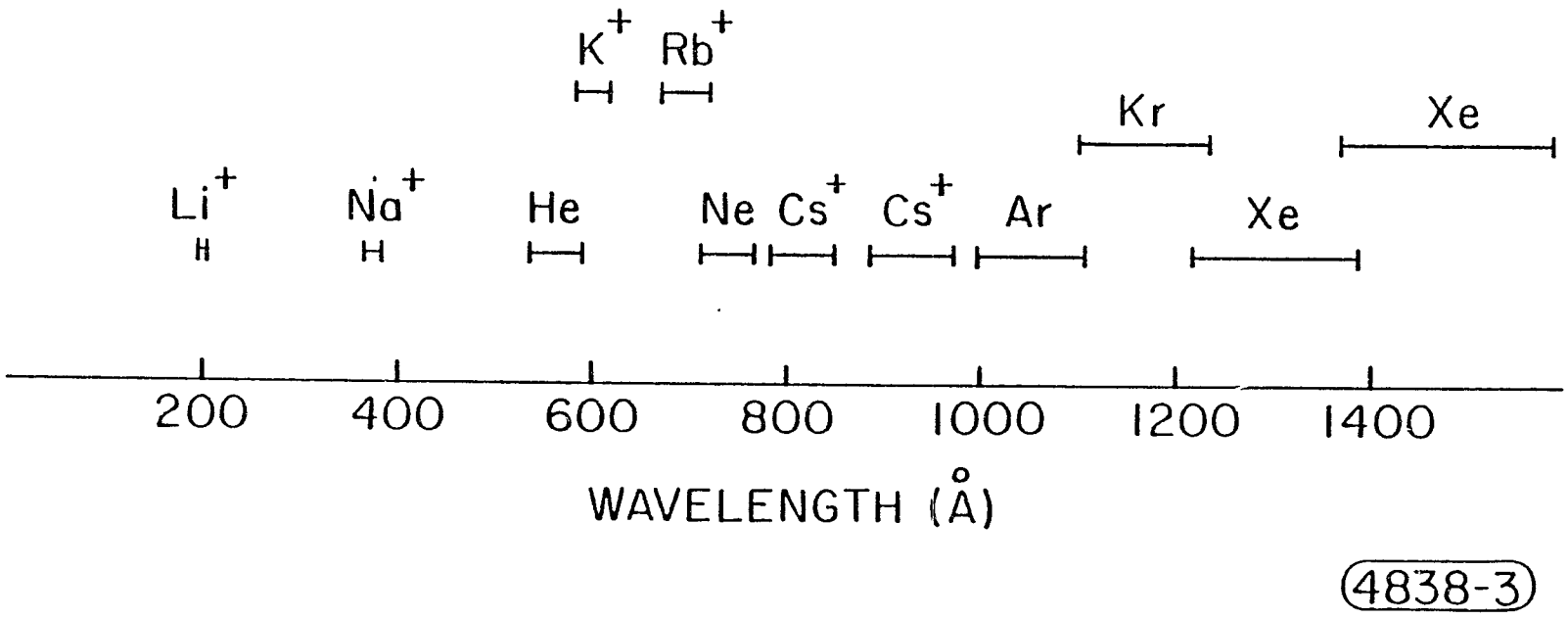

Fig. 12--Possible spectral regions which could be examined using the spontaneous Raman source.

V. CONCLUSION

The experiments described in this paper have shown that the spontaneous Raman anti-Stokes radiation source may be used to obtain very high resolution over limited spectral regions. The complexity of changing the storage species will limit the source to situations where features have been previously identified with lower resolution apparatus. Very often it is the case that the center wavelength which is obtainable from an ionic species, for example, 601 Å from K II (Table 7), coincides with the region of most interest for studying the core-excited spectrum of the neutral species. For example, if one is able to obtain ± 15,000 cm^{-1} of tuning centered at 601 Å, this would cover the spectral region from 551 Å to 660 Å. This would allow examination of a good portion of the interesting spectral region of K I.

Other properties of the spontaneous Raman anti-Stokes radiation source which may be useful are its controlled polarization and the ability to produce pulses as short as that of the incident laser.

The ultimate usefulness of this source will depend on the development of convenient methods for producing large metastable populations. Two promising approaches are the pulsed hollow cathode technology demonstrated by Falcone, et al. [7] and metastable production by photoionization with laser produced soft x-rays [8].

ACKNOWLEDGEMENTS

The authors gratefully acknowledge contributions to this work by E. Kintzer and D. Holmgren, and technical assistance by B. Yoshizumi. J. E. Rothenberg also gratefully acknowledges the support of the Fannie and John Hertz Foundation.

REFERENCES

[1] M. L. Ginter, D. S. Ginter, and C. M. Brown, "Need for high resolution in VUV Rydberg state spectroscopy," Appl. Opt., vol. 19, pp. 4015-4020, Dec. 1980.

[2] S. E. Harris, "Spontaneous anti-Stokes scattering as a high-resolution and picosecond-time-scale VUV light source," Appl. Phys. Lett., vol. 31, pp. 498-500, Oct. 1977.

[3] Joshua E. Rothenberg, J. F. Young, and S. E. Harris, "High-resolution extreme-ultraviolet spectroscopy of potassium using anti-Stokes radiation," Opt. Lett., vol. 6, pp. 363-365, Aug. 1981.

[4] R. W. Falcone, J. R. Willison, J. F. Young, and S. E. Harris, "Measurement of the He 1s2s $^1S_0$ isotopic shift using a tunable VUV anti-Stokes light source," Opt. Lett., vol. 3, pp. 162-163, Nov. 1978.

[5] P. Bräunlich and P. Lambropoulos, "Detection of singly stimulated two-photon emission from metastable deuterium atoms," Phys. Rev. Lett., vol. 25, pp. 135-318, July 1970; and "Anti-Stokes Raman scattering from metastable deuterium atoms," Phys. Rev. Lett., vol. 25, pp. 986-987, Oct. 1970.

[6] L. J. Zych, J. Lukasik, J. F. Young, and S. E. Harris, "Laser-induced two-photon blackbody radiation in the vacuum ultraviolet," Phys. Rev. Lett., vol. 40, pp. 1493-1496, June 1978.

[7] R. W. Falcone and K. D. Pedrotti, "Pulsed hollow-cathode discharge for extreme-ultraviolet lasers and radiation sources," Opt. Lett., vol. 7, pp. 74-76, Feb. 1982.

[8] R. G. Caro, J. C. Wang, R. W. Falcone, J. F. Young, and S. E. Harris, "Soft x-ray pumping of metastable levels of Li^+," Appl. Phys. Lett., vol. 42, pp. 9-11, Jan. 1983.

[9] V. L. Jacobs and J. Mizuno, "Interaction of laser light with the 2^1S_o metastable state of helium," J. Phys. B: Atom. Molec. Phys., vol. 5, pp. 1155-1159, June 1972.

[10] E. Courtens and A. Szöke, "Time and spectral resolution in resonance scattering and resonance fluorescence," Phys. Rev. A, vol. 15, pp. 1588-1603, April 1977.

[11] Yu. M. Kagan and A. S. Taroyan, "Excitation of helium in a hollow-cathode discharge — Part 1," Opt. Spect., vol. 35, pp. 120-123, Aug. 1973.

[12] G. N. Steele, "XUV filters: Out of this world and back again," Opt. Spectra, vol. 10, pp. 37-40, June 1976.

[13] R. B. Cairns and J. A. R. Samson, "Metal photocathodes as secondary standards for absolute intensity measurements in the vacuum ultraviolet," J. Opt. Soc. Amer., vol. 56, pp. 1568-1573, Nov. 1966.

[14] G. Herzberg, "Ionization potentials and Lamb shifts of the ground states of ^4He and ^3He," Proc. Roy. Soc. London A, vol. 248, pp. 309-332, Nov. 1958.

[15] W. C. Martin, "Energy levels and spectrum of neutral helium (^4He I)," J. Res. Nat. Bur. Stand., vol. 64A, pp. 19-28, Jan.-Feb. 1960.

[16] M. W. D. Mansfield, "The K I absorption spectrum in the vacuum ultraviolet: 3p-subshell excitation," Proc. Roy. Soc. London A, vol. 346, pp. 539-553, Nov. 1975.

[17] M. W. D. Mansfield and T. W. Ottley, "The identification of low energy K and Ca^+ autoionizing levels observed in electron impact experiments," Proc. Roy. Soc. London A, vol. 365, pp. 413-424, March 1979.

[18] G. Kavei, T. W. Ottley, V. Pejcev, and K. J. Ross, "High resolution ejected-electron spectra of K I and K II autoionizing levels excited by low-energy electron impact on potassium vapor," J. Phys. B: Atom. Molec. Phys., vol. 10, pp. 2923-2933, Oct. 1977.

[19] V. S. Borodin and Yu. M. Kagan, "Excitation of helium in a hollow-cathode discharge," Opt. Spect., vol. 23, pp. 108-110, July 1967.

[20] Joshua E. Rothenberg and Stephen E. Harris, "XUV lasers by quartet to doublet energy transfer in alkali atoms," IEEE J. Quantum Electron., vol. QE-17, pp. 418-422, March 1981.

[21] J. C. Wang and R. Normandin, unpublished data.

[22] T. Sasaki, H. Fukutani, K. Ishiguro, and T. Izumitani, "Determination of optical constants of glasses in the vacuum ultraviolet region," Japanese J. Appl. Phys., vol. 4, supplement 1, pp. 527-531, 1965.

[23] U. Fano, "Effects of configuration interaction on intensities and phase shifts," Phys. Rev., vol. 124, pp. 1866-1878, Dec. 1961.

[24] R. D. Hudson and V. L. Carter, "Experimental values of the atomic absorption cross section of potassium between 580 Å and 1000 Å," J. Opt. Soc. Amer., vol. 57, pp. 1471-1474, Dec. 1967.

[25] R. S. Van Dyck, Jr., C. E. Johnson, and H. A. Shugart, "Lifetime lower limits for the $^3P_0$ and $^3P_2$ metastable states of neon, argon, and krypton," Phys. Rev. A, vol. 5, pp. 991-993, Feb. 1972.

[26] J. R. Willison, R. W. Falcone, J. F. Young, and S. E. Harris, "Laser spectroscopy of metastable extreme-ultraviolet levels in lithium atoms and ions," Phys. Rev. Lett., vol. 47, pp. 1827-1829, Dec. 1981.